NASA TECHNICAL NOTE

NASA TN D-2708

c. 1

NASA TN D-2708

A STUDY OF PRESSURE AND HEAT TRANSFER OVER AN 80° SWEEP SLAB DELTA WING IN HYPERSONIC FLOW

by Allen H. Whitehead, Jr., and James C. Dunavant

Langley Research Center
Langley Station, Hampton, Va.

NATIONAL AERONAUTICS AND SPACE ADMINISTRATION • WASHINGTON, D. C. • MARCH 1965

A STUDY OF PRESSURE AND HEAT TRANSFER OVER AN 80° SWEEP SLAB DELTA WING IN HYPERSONIC FLOW

By Allen H. Whitehead, Jr., and James C. Dunavant

Langley Research Center
Langley Station, Hampton, Va.

NATIONAL AERONAUTICS AND SPACE ADMINISTRATION

For sale by the Office of Technical Services, Department of Commerce,
Washington, D.C. 20230 -- Price $2.00

A STUDY OF PRESSURE AND HEAT TRANSFER
OVER AN 80° SWEEP SLAB DELTA WING
IN HYPERSONIC FLOW

By Allen H. Whitehead, Jr., and James C. Dunavant
Langley Research Center

SUMMARY

An experimental investigation has been conducted to obtain heat-transfer and pressure distributions over an 80° swept slab delta wing at Mach numbers of 6.8 and 9.6 in air. The wing had cylindrical leading edges, a hemispherical nose of the same radius, and a length of 7.12 nose diameters. The angle of attack varied from 0° to 35°. Reynolds numbers of 9.9×10^4 and 37.0×10^4 based on model thickness were obtained at Mach 6.8, and a Reynolds number of 10×10^4 was employed for the Mach 9.6 tests.

The nose greatly influenced the flow behavior over the leading-edge region at low angles of attack. Two results of this apex influence were apparent in the pressure distribution over the leading edge of the 80° swept wing. An empirical swept-cylinder theory greatly overpredicted the pressure level over the leading edge of the 80° swept wing. There was also a characteristic decrease in the pressures down the leading edge of the 80° swept wing in contrast to the nearly constant pressure level in the same region of a lower swept delta wing. The heat-transfer distribution over the leading-edge region of the 80° swept wing was similarly influenced by the nose region geometry. As angle of attack increased, the nose influence diminished and the heat-transfer and pressure distributions over the leading edge of the 80° swept wing conformed to the two-dimensional swept-cylinder behavior exhibited by the lower swept wings at all angles of attack.

Constant-pressure strip theory predicts the heat transfer correctly over the slab portion of the delta wing only for the intermediate angles of attack. At low angles of attack, the flow is not chordwise and thus does not meet the criteria for strip theory. At the highest angles of attack, the flow turns outward over the slab, and crossflow theory gives the approximate level of the heating in the center-line region.

Transition appears to occur on the trailing edge of the wing at the highest angles of attack. The heat-transfer values in this region are twice the experimental laminar flow values.

INTRODUCTION

Extensive experimental and theoretical studies have been made on the delta wing because of its potential use as a glider and a reentry vehicle. Such a vehicle must be designed to cover a wide angle-of-attack range; during reentry, high angles of attack are required to decelerate, whereas lower angles of attack produce more favorable maneuver characteristics. The delta-wing configuration can satisfy these criteria and also has inherent stability.

Aerodynamic heating of a hypervelocity vehicle presents a major problem in the design. The bluntness can be increased and the leading edge can be swept back to a higher degree to reduce the heating in the critical areas of the nose and leading edge. Increasing the sweep of the leading edge also reduces the bluntness-induced drag (refs. 1 and 2). Reports of previous investigations of highly swept, blunt delta wings are available (refs. 3 to 9), but most of this literature is concerned with sweep angles of 70° and lower. The present investigation of an 80° swept blunt-leading-edge delta wing was undertaken as part of a systematic research program initiated at Langley Research Center to provide analyses of the aerodynamic heating, the pressure distribution, and the flow patterns over blunt delta wings.

SYMBOLS

c_w	specific heat of model skin material
d	nose diameter; leading-edge diameter
h	aerodynamic heat-transfer coefficient
L	distance along leading edge measured from apex of slab portion of wing
M	Mach number
N_{Pr}	Prandtl number
N_{St}	Stanton number
p	static pressure
p'	static pressure behind normal shock
q	heat-flow rate per unit area
r	nose radius
$R_{\infty,t}, R_{\infty,d}$	Reynolds number based on model thickness or nose diameter and free-stream conditions

s_c	distance from geometric stagnation point along surface at center line
s_o	distance along wing surface normal to leading edge from midline of wing
t	model thickness
t_{eff}	effective skin thickness
t_w	model skin thickness
T	temperature
x	coordinate parallel to center line from apex stagnation point
y	distance from center line to leading-edge shock measured perpendicular to center line
α	angle of attack
γ	ratio of specific heats of air
η	temperature-recovery factor
θ	initial deflection angle at a point on wing slab measured outward from a line parallel to center line
Λ	sweep angle
ρ_w	density of model skin material
τ	time
φ	angular measure in plane normal to leading edge from midline of wing (see fig. 1)

Subscripts:

c	conduction term
e	adiabatic wall conditions
l	local static conditions just outside boundary layer
o	stagnation-point values
s	sphere; storage term
w	model skin
∞	undisturbed free-stream conditions

APPARATUS AND TESTS

Wind Tunnel

The investigation was conducted in the Langley 11-inch hypersonic tunnel described in reference 10. The facility is of the blowdown type with test durations of about a minute. Nominal Mach numbers of 6.8 and 9.6 with air as the test medium were obtained with two interchangeable nozzles. The Mach number 6.8 nozzle is a contoured two-dimensional nozzle constructed from invar so that contraction and expansion of the throat due to extreme temperatures is minimized. The Mach number 9.6 nozzle is a contoured three-dimensional nozzle with a square throat and test section machined from steel. The nozzle calibrations show that stagnation pressure has a slight effect on the Mach number. The Mach number variation during the test run is only about 1 percent after the first 10 seconds. Calibrations of the two nozzles may be found in references 11 and 12.

Models and Instrumentation

The configuration was an 80° swept delta wing with a cylindrical leading edge which was tangent to a flat slab on the upper and lower surfaces. The blunt nose was a hemisphere with the same diameter as the leading edge (1.00 inch). Details of the model and instrumentation are presented in figure 1.

Three models were used to obtain oil-flow, heat-transfer, and pressure data for the 80° swept configuration. The oil-flow model was machined from a solid piece of mild steel. The heat-transfer model, with approximately 0.031-inch skin thickness, was constructed from inconel. Measurements of the skin thickness were obtained at each thermocouple location for use in data reduction. The thermocouples on the heat-transfer model were number 30 chromel-alumel wire and were spot welded to the inner skin. Time histories of the tunnel stagnation temperature and the model skin temperatures were obtained on 18-channel recording galvanometers. Internal resistances were adjusted to give as near full-scale deflection as possible at each location. The pressure orifices through the skin had 0.040-inch inside diameters. The pressure leads were subsequently directed through the model support system to the recording instruments outside the tunnel. The pressure recorders were six-cell aneroid-type units which are described in more detail in reference 10. The accuracy of the units is ±1/2 percent of full-scale deflection. Pressure cells were selected to give as near a full-scale deflection as possible during the run.

Tests

Heat-transfer data, pressure data, and surface-flow data were obtained at Mach numbers of 6.8 and 9.6 in air. The model was tested at angles of attack from 0° to 35°. Stagnation temperatures were maintained near 650° F at $M_\infty = 6.8$ and 1200° F at $M_\infty = 9.6$ in order to prevent liquefaction of the air during the tests. The tests at $M_\infty = 6.8$ were run at stagnation pressures of 9 and 35 atmospheres, which resulted in Reynolds numbers of 9.9×10^4 and

37.0×10^4, based on model thickness. The stagnation pressure for the tests at Mach 9.6 was 45 atmospheres, and yielded a Reynolds number of about 10×10^4. The water vapor content in the air was maintained at less than 1.87×10^{-5} pound of water per pound of dry air so that water-condensation effects would be eliminated.

Surface flow patterns were obtained by using the oil-flow technique. Before the run, a mixture of oil and lampblack was applied to the oil-flow model in a dot pattern. The direction and extent of the flow of the oil droplets during the tunnel run allow a qualitative analysis of the surface flow over the model. Schlieren photographs were taken simultaneously with the heat-transfer and pressure data at each angle of attack.

Data Reduction

The local heat-transfer rate to the model was determined from a skin heat balance which included the heat stored in the skin and the heat conducted laterally along the skin. The heat lost through radiation was negligible. For a model with a thin skin, the flow of heat to the model per unit area is given by

$$q = q_s + q_c \tag{1}$$

where $q_s = \rho_w c_w t_{eff} \frac{dT_w}{d\tau}$. The effective skin thickness t_{eff} is determined for the curved portion of the leading edge by

$$t_{eff} = t_w\left(1 - \frac{t_w}{d}\right) \tag{2}$$

and for the sphere nose region by

$$t_{eff} = t_w\left[1 - 2\left(\frac{t_w}{d}\right) + \frac{4}{3}\left(\frac{t_w}{d}\right)^2\right] \tag{3}$$

The time derivative of the wall temperature was obtained by manually reading the slope of the recorded thermocouple outputs. The slope was read as soon as flow conditions of stagnation temperature and pressure stabilized, about 2 seconds after the start of the flow. The model was initially isothermal but during this 2-second interval the model wall temperature in some locations rose sufficiently to permit conduction of a substantial amount of heat laterally along the model. Hence, the measured heat-storage term was corrected by a heat-conduction term determined from the measured wall temperatures and the three-point finite-difference method of reference 5. In the critical regions of the wing nose and leading edge, the conduction term was the same order of magnitude as the storage term. Over the slab portion of the wing, the conduction accounted for only a small percent of the heat transfer. The local heat-transfer coefficients were obtained from

$$q = h\left(T_e - T_w\right) \tag{4}$$

The adiabatic wall temperatures T_e were obtained from

$$\frac{T_e}{T_o} = \frac{1 + \eta\frac{\gamma - 1}{2}M_l^2}{1 + \frac{\gamma - 1}{2}M_l^2} \tag{5}$$

Local Mach number M_l at the edge of the boundary layer can be related to the surface pressure when the entropy level of the streamline at the edge of the boundary layer is known. The entropy rise is a function of the angle of the shock through which the streamline has passed. On the basis of the schlieren photographs, at $\alpha = 0^{\circ}$ and $\alpha = 5^{\circ}$ all streamlines were assumed to have passed through the normal shock at the nose. At angles of attack of 10° and above, a normal shock was assumed for the sphere nose region, and an oblique shock parallel to the slab portion of the wing was used for the remainder of the wing. The laminar recovery factor η was evaluated for the laminar boundary layer as

$$\eta = \left(N_{Pr}\right)^{1/2}$$

the Prandtl number was calculated at the reference temperature obtained from Monaghan's T-prime method. (See ref. 14.)

RESULTS AND DISCUSSION

Visual Flow Studies

Oil flow.- The oil-flow variation of the surface streamlines with angle of attack at $M_\infty = 6.8$ is presented in figures 2 and 3. Plan- and side-view photographs of the model with the oil-flow traces are shown in figure 2. The composite oil-flow sketch in figure 3 shows the variation of the traces with angle of attack for two stations on the slab portion and for stations along the leading edge of the wing.

At $\alpha = 0^{\circ}$ the surface streamlines along the cylindrical leading edges show a definite flow toward the center of the wing, which is the direction of the lateral pressure gradient. On the flat slab portion of the wing at this angle of attack, the oil flow is outward in a direction contrary to the pressure gradient and flow direction over the leading edge. The two flows intersect approximately at the juncture of the cylindrical leading edge and the wing slab. The intersection shows best on the right-hand side of the $\alpha = 0^{\circ}$ photograph where the oil flow is indicated by a single dashed line running parallel to the leading edge. The outflow on the slab is explained by Bertram in reference 5 as a consequence of the mass of air at high induced pressures which enters the wing over the apex region and is contained by the shock, the wing surface, and the high pressure induced in the air coming from the leading-edge region. Dissipation of this nose effect occurs as this flow moves further downstream.

As the angle of attack increases, the velocity component normal to the slab increases and thus causes the high pressure over the blunt apex to expand to a relatively higher pressure on the wing surface. The outflow caused by the expansion of the flow over the blunt nose at low angles of attack diminishes as angle of attack increases. The oil flow over the slab moves inward toward the center line for $\alpha = 5^\circ$, 10°, and 15°. As angle of attack further increases, the increased normal component apparently equalizes the effects of the leading-edge pressure gradient, and at $\alpha \approx 30^\circ$, the flow is essentially conical except for the bluntness effect at the leading edge. At higher angles of attack, the flow diverges increasingly from the center of the wing; this crossflow apparently turns some of the streamlines outward to such an extent that the geometrical leading edge becomes a trailing edge to the flow. The composite oil-flow sketch (fig. 3) best identifies these flow regimes. In figure 3(a) oil-flow streamlines have been sketched from the photographs of figure 2 for two stations at different locations on the wing. The station near the shoulder of the hemisphere-cylinder leading edge naturally shows the widest variation of θ with α. The accompanying plot shows the general variation of θ with α. Evidently, θ decreases with α until the crossflow component becomes large enough to overcome the effect of the leading-edge bluntness, and then the flow turns outward. The leading-edge oil flow is schematically represented in figure 3(b). The dotted lines on these sketches show the location of the theoretical stagnation line on an isolated swept cylinder for comparison with the variation of flow on the leading edge of the delta wing.

Schlieren photographs.- Figure 4 presents side-view schlieren photographs of the 80° swept wing at varying angles of attack for the two Mach numbers. The shock shapes for the two Mach numbers show no dissimilarities. Although the photographs are not included, the shock shapes produced during the Mach 6.8 tests with a different Reynolds number were similar to the shock shapes shown in figure 4(a).

The apex shock is characteristic of that produced by a sphere, whereas the shock over the rear portion is representative of the shock from a flat plate. At the higher angles of attack the interaction of these two effects produces an inflection in the bow-shock curvature which occurs about 1 or 2 diameters back from the nose. A similar phenomenon was observed in reference 5 for a 70° swept wing.

In the Mach number 9.6 nozzle at $\alpha = 35^\circ$, the model has reached an angle of attack where boundary-layer separation from the tunnel wall is induced. The $\alpha = 35^\circ$ photograph of figure 4(b) shows the shock from this wall separation striking the body near the trailing edge. The heat-transfer and pressure data corresponding to this schlieren picture are included in the report because the values upstream of the point of intersection of the shock with the model appear to be unaffected by the phenomenon.

Figure 5 presents top-view schlieren photographs at Mach 6.8 of geometrically similar delta wings with different sweep angles. In addition to the 80° swept wing under study are photographs of a 70° swept wing (ref. 5) and photographs of a hemisphere-cylinder obtained in the investigation reported in reference 14. In this view, a significant difference is seen in the behavior of the shock about the models. For the 70° swept wing, the shock downstream of the inflection point bends toward the leading edge and then over a significant part of the body runs almost parallel to the leading edge. The leading edge thus determines the shock shape past the inflection point, and the transverse flow is expected to be similar to that over a swept cylinder. In contrast, the schlieren photographs shown in figure 5 for the 80° and 90° swept wings reveal a very different behavior of the shock behind the nose. For the wing length of the 80° swept wing and for the indefinite length of the 90° swept wing, the wing sweep has increased to the point where the shape of the shock produced at the blunt apex is not affected by the presence of the leading edge. As a result, there is no plan-view inflection point and the shock wave behind the nose is no longer parallel to the leading edge. Of course, if the length of the 80° swept wing were extended, the leading edge would eventually interact with the nose shock when the nose shock began to dissipate toward a Mach line. Figure 6 was prepared from leading-edge shock detachment distances obtained from the top-view schlieren pictures in figure 5 and from an unpublished top-view schlieren photograph of a 45° swept delta wing run at a Mach number of 20 in the Langley 22-inch helium tunnel. The results of this figure clearly show that when the shock distance from the model center line is normalized by dividing by the nose radius, the shock shapes produced by the 80° swept delta wing and the hemisphere-cylinder almost coincide. Thus the assumption that the leading edge of the highly swept 80° delta wing has negligible effect on the shock shape for this Mach number and wing length is justified. With the leading edge thus in the shadow of the nose shock, the flow in the leading-edge region is no longer uniquely determined by the geometry of the leading edge. The implications of this phenomenon for pressure and heat-transfer distributions are discussed later. In contrast, the shock shapes of the 45° and 70° swept delta wings are strongly affected by the sweep angle (and hence the presence of leading edge) as evidenced in figure 6 by the dissimilarity of the faired shock curves for these wings from that of the hemisphere-cylinder. The condition under which the leading edge falls in the shadow of the nose shock appears to be a function of at least four factors: the wing sweep, the free-stream Mach number, the magnitude of the nose bluntness, and, of course, the wing length.

Pressure Distribution

Center-line pressure.- The center-line pressure distribution over the 80° swept wing at the two test Mach numbers is presented in figure 7. The abscissa s_c/t is in a form which varies with angle of attack since the orifice location is measured from the geometric stagnation point on the spherical nose. Newtonian theory applied to the nose region reasonably predicts the data almost up to the tangency point between the sphere nose and the slab region. (See dotted vertical line in fig. 7.) The data on the slab at zero angle of attack are compared with pressures obtained by the method of Creager (ref. 15), which includes boundary-layer displacement effects and inviscid blast-wave effects.

This method considerably overpredicts the pressures. Similar to the effect observed for a wing geometrically similar to that tested herein but with a 70° wing sweep (ref. 5), the pressure gradient on the slab portion of the wing is very pronounced at the lowest angles of attack but practically disappears for angle of attack of 20° and greater. The free-stream static-pressure ratio is included on the figure for reference.

The center-line data for Mach 6.8 presented in figure 7(a) shows that quadrupling the value of the Reynolds number has only a small effect on the pressure distribution. The maximum differential, which occurs at $\alpha = 0^\circ$, is about 10 percent.

Figure 8(a) presents center-line data at Mach number 9.6 for two highly swept slab delta wings and a hemisphere-cylinder (90° sweep angle). The 80° swept wing is the model under study herein; the data for the 70° and 90° swept wings have been obtained from references 5 and 6, respectively. As predicted from a consideration of the blast-wave concept of the leading-edge contribution to the pressures on the slab surface, the lower swept wing at all angles of attack experiences the highest pressures along the center line of the slab portion of the wing. As the wing sweep increases, the tendency for the high pressures on the windward side of the model to bleed around to the leeward side also increases.

Leading-edge pressure distribution.- Figure 8(b) presents the leading-edge pressure distribution along the theoretical swept-cylinder stagnation line for the same three highly swept configurations in figure 8(a). Experimental pressure values were available for all wings at $\alpha = 0^\circ$ and for the 80° swept wing at $\alpha = 15^\circ$; for the remaining three cases, the pressures on the rotated stagnation line were obtained by fairings through the actual data points. For any selected L/t value along the leading edge, the wing with the lower sweep experiences the higher pressure. A more striking difference due to wing sweep in the pressure variation over the wings at zero angle of attack occurs in the distribution of the pressures down the leading edge. About 3 diameters back from the nose of the 70° swept wing, the pressure level is almost constant and is adequately predicted by swept-cylinder theory. For the 80° swept wing, however, the flow over the leading edge is three dimensional in nature, evidenced by the strong pressure gradient existing to the limit of the instrumentation ($L/t = 6$); in this region the two-dimensional swept-cylinder theory is clearly inadequate. This pressure gradient down the leading edge of the more highly swept model is a consequence of the phenomenon observed in the top-view schlieren photographs of figure 5. As mentioned in the discussion of figures 5 and 6, for the 80° swept wing and the hemisphere-cylinder at $\alpha = 0^\circ$ the leading edge lies in the shadow of the apex shock; hence, the effectiveness of the leading edge in controlling the flow in this region is expected to be strongly reduced. In contrast, the leading edge of the 70° swept wing intercepts the nose shock and the shock just past the nose runs nearly parallel to the leading edge, and thus simulates the effects of a swept cylinder.

As angle of attack increases to 15°, the leading-edge pressures on the 80° swept wing are suitably predicted by swept-cylinder theory for $L/t \geqq 4$. The induced effects from the nose still provide the major influence on the pressures over the forward portion of the leading edge. The crossflow theory predicts the trend of the pressures over the 70° swept wing for $L/t \geqq 3$. At $\alpha = 30^\circ$, the pressures down the leading edge of both wings show only a slight variation, and theory predicts the levels very well.

Pressure distribution on wings at zero angle of attack.- The measured pressure distributions normal to the leading edge of the 80° swept wing at angles of attack for Mach numbers 6.8 and 9.6 are presented in figures 9 and 10, respectively. At angles of attack of 0°, 15°, and 30°, pressure distributions over a geometrically similar slab delta wing with a 70° sweep angle (ref. 5) are included for $M_\infty = 9.6$ in figure 10. The juncture of the cylindrical leading edge and the slab region occurs at $s_o/t = 0.785$ and appears at the bottom of figures 9 and 10 as a short-dashed vertical line. Comparison of figures 9(a) and 9(b) reveals that there is only a slight Reynolds number effect on the pressure distribution.

In figure 10(a), the measured pressure distributions are presented for $\alpha = 0^\circ$ on the 70° and 80° swept wings at Mach 9.6. The pressure dispersion in the leading-edge region $\left(s_o/t \leqq 0.785\right)$ of the 80° swept wing is again in sharp contrast to the pressure variation in the same region over the 70° swept wing. For the lower swept wing at stations sufficiently downstream of the nose influence, the leading-edge pressures coalesce into a single band whose trend is reasonably predicted by the swept-cylinder correlation found in reference 5. As discussed previously, at $\alpha = 0^\circ$ the nose influence predominates over the entire leading-edge region of the 80° swept wing.

Another observation to be made from figure 10(a) is also a result of the decreased influence of the leading edge in determining the flow behavior over the 80° swept wing. The detached two-dimensional shock produces a large spanwise pressure gradient normal to the leading edge of the 70° swept wing. The slope of the pressure distribution at a chosen station is a measure of the magnitude of this effect at any spanwise location. In strong contrast, the pressure distribution normal to the leading edge of the 80° swept wing is nearly constant for stations downstream of the nose. Some leading-edge influence remains, however, as seen by the curvature of the pressure distribution on the shoulder $\left(s_o/t = 0.785\right)$, but the effect has been strongly attenuated.

Pressure distribution on wings at intermediate and high angles of attack.- The leading-edge pressure distribution over the 80° swept wing in figure 8(b) suggests closer agreement with the swept-cylinder theory as angle of attack increases beyond 15°. This trend is confirmed for $\alpha \geqq 20^\circ$ in figures 9 and 10, in which the spanwise pressure distributions at the various stations coalesce toward the swept-cylinder correlation.

The pressure level on the slab portion is approximately 10 percent higher on the 70° swept wing than on the 80° swept wing. Three theories, which predict the asymptotic values of the pressures over the slab portion of the delta wings, are presented in figures 9 and 10. Oblique-shock theory is based on the two-dimensional sharp leading-edge flat plate which is positioned at the same angle of attack as the wing. The Newtonian theory is based on the slab inclination, and the tangent-cone theory provides the theoretical distribution over a three-dimensional pointed cone with a semiapex angle equal to the wing angle of attack. Oblique-shock and Newtonian theory provide upper and lower boundaries, respectively, for the experimental data of both wings. Tangent-cone theory falls between these boundaries and for $\alpha \geqq 10^\circ$ this theory well predicts the pressures on the 80° swept wing near the center line.

The variation of the pressure distribution with angle of attack for the 80° swept wing at Mach 9.6 is better seen in figure 11. This figure was constructed to facilitate the study of the flow behavior at a selected station by plotting p_w/p_∞ against s_o/t at each L/t station for the range of angle of attack. Angle-of-attack fairings have been drawn through the data. At each angle of attack, the short-dashed vertical lines on figure 11 indicate the theoretical spanwise location $\left(s_o/t \text{ value}\right)$ of the swept-cylinder stagnation point. The center-line distance from the leading-edge midline which varies from station to station is included on each figure for reference. For all stations at $\alpha \leqq 15^\circ$, the data fairing suggests that the location of the maximum value of the experimental pressure is at the s_o/t value predicted by two-dimensional, swept-cylinder theory. As angle of attack increases to 20°, the stagnation line has moved past the spanwise location predicted by the swept-cylinder theory, and for angles of attack of 25° and above, the stagnation line occurs at the center line. This behavior of the stagnation line is verified by the oil-flow patterns in figure 2.

Heat-Transfer Distribution

Effect of sweep at $\alpha = 0^\circ$.- Distributions of the heat-transfer parameter $\left(N_{St,\infty}\sqrt{R_{\infty,t}}\right)$ at $\alpha = 0^\circ$ along the center lines and the leading-edge stagnation line of three models with sweeps of 70°, 80°, and 90° are shown in figure 12. The heat-transfer data for the 70° swept wing are from reference 5; for the 80° swept wing, from the present investigation; and for the 90° swept wing, from reference 13. At station $L/t = 0$ for the center line the data should coincide with the result for the 90° station on a hemisphere. However, for the leading edge at $L/t = 0$, the results correspond to 70°, 80°, and 90° stations on a hemisphere for the 70°, 80°, and 90° sweeps, respectively. The changing levels of heat transfer in the region of $L/t = 0$ reflect this fact. This behavior also applies to the pressure data presented in figure 8. Along the center line the heating for the 70° and 80° swept wings appears to be lower than that for the 90° swept wing or hemisphere-cylinder model, although the small amount and possible scatter of the data for the 70° and 80° swept wings makes the trends difficult to discern. This apparent trend in level of heating on the center line is opposite to that of the pressures where, as shown in figure 8(a), the lowest surface pressures were measured at a 90° sweep and the highest at a 70° sweep.

The variation of the levels of heating along the leading edges shown in figure 12(b) for the three sweeps is similar to that of the level of pressure shown in figure 8(b), that is, the pressure and heating on the 70° sweep leading edge is highest and that on the 90° sweep is lowest. The pressure decrease along the leading edge (increasing L/t), which occurs only for the 80° and 90° sweeps (fig. 8(b)), is more marked than the decrease in heating shown in figure 12(b). The pressure and the heat transfer along the leading edge of the 70° swept wing show little change along the leading edge.

Leading-edge region.- The theoretical values of the heat-transfer parameter $\left(N_{St,\infty}\sqrt{R_{\infty,d}}\right)_o$ for the stagnation line along the leading edge can be obtained from the modification of the Fay and Riddell theory (ref. 16) found in reference 5. This theory was used in figure 13 to predict the experimental heating on the swept leading edges of the 70° (ref. 5) and 80° swept delta wings. The solid curve in this figure is the theory for the 70° swept wing, and the long-dashed line that for the 80° swept wing. The filled symbols are the maximum experimental values (obtained near the geometric stagnation line) of the heat-transfer parameter along the leading edge of the 70° swept wing; the open symbols are the corresponding stagnation values for the 80° swept wing obtained in the same manner as the stagnation-line pressures of figure 8(b). The heat-transfer parameter is plotted against angle of attack for five stations along the leading edge. In general, the values of the heat-transfer parameter are above the predicted values of the Fay and Riddell theory for the 70° swept wing, but below the theory for the 80° swept wing. This reversal of the relationship between data and theory for the two wings is thought to be a consequence of the phenomenon observed in the top-view schlieren photographs of figure 5 and discussed in the section on schlieren photographs. Because the leading edge of the 80° swept wing lies in the shadow of the shock from the nose, the heat transfer in the leading-edge region is lower than that expected for the infinite swept cylinder model assumed in the Fay and Riddell theory. The shock along the leading edge of the 70° swept wing, however, is similar to the shock produced by the swept cylinder. Further substantiating this reasoning is the trend of the Fay and Riddell theory for the 80° swept wing when the experimental pressures are used in the theory. The theory with experimental pressures is shown in figure 13 as a short-dashed line, and it follows the data for the 80° swept wing more closely than the theory with theoretical pressures employed.

Center-line heat transfer.- Figure 14 presents the variation in the heating down the center line of the 80° swept wing for Mach 9.6 expressed as a fraction of the theoretically predicted heating at the apex stagnation point. The data are again displaced for the shift of the stagnation point in this figure. The following theoretical apex stagnation values of the heat-transfer parameter were obtained from the three-dimensional Fay and Riddell theory for the nominal test conditions:

M_∞	$\left(N_{St}\sqrt{R_{\infty,d}}\right)_{o,s}$
6.8	6.84
9.6	9.10

The center-line heat transfer at Mach 6.8 was not plotted because the heating in this region did not vary significantly with Mach number.

The heat transfer over the hemispherical nose is predicted by Lees' theory (ref. 17) and has been plotted in figure 14. Two apex stagnation-region thermocouples were lost during the tests; therefore, the data are incomplete in the nose region. Those data values that do appear, however, are well predicted by Lees' theory.

Lees' theory was also used to predict the heating beyond the nose region by using the measured pressures on the slab and by assuming the flow on the slab to be two dimensional. This theory is compared with the data in figure 14 for $\alpha = 0^\circ$, 15°, and 30°. This theory greatly overestimates the heating at $\alpha = 0^\circ$ but agrees well at $\alpha = 30^\circ$.

For low and intermediate angles of attack, the oil-flow studies and pressure data suggest that the flow over the slab portion of the wing can be considered to be composed of chordwise strips. Strip theory in figure 14 predicts the center-line heating distribution over the 80° swept wing best at $\alpha = 20^\circ$. The zero pressure-gradient strip theory appearing in the center-line heating distribution of reference 5 was inconsistently based on the chordwise distance along a windward cross section of the leading edge (elliptic nose shape) rather than along the center-line cross section (semi-circular nose shape). Thus the curvature and level of the strip theory that appears in figure 14 of the present study differs from that found in figure 10 of reference 5.

The apex-induced effect noted for the 70° swept-wing center-line heating distribution of reference 5 is also apparent for the 80° swept wing. The magnitude of the effect can be qualitatively estimated by observing the slope of the data in the center-line region behind the shoulder of the nose. To predict better the heating at $\alpha = 0^\circ$ where bluntness-induced effects are large, strip theory has been modified for pressure, pressure gradient, and nose geometry. (See ref. 14.) This modified theory appears in figure 14 as a short-dashed curve and is seen to predict more closely the heating in the region immediately behind the nose where induced effects are strongest. As angle of attack increases, the magnitude of the induced pressure decreases, and the distance over which the nose-induced effect is significant also decreases. (See fig. 7.)

As angle of attack increases, the effects of spanwise flow become more significant and strip theory falls below the data. As the oil-flow studies have suggested, as angle of attack increases above about 20°, the component of velocity normal to the wing begins to turn the streamlines outward from the center line. Within this spanwise flow regime the heat-transfer data can be suitably predicted by crossflow theory, which is an adaptation of the Fay and Riddell relation for stagnation-point heating taken from reference 5. In Bertram's development of this theory, the component of the free-stream flow normal to the slab portion of the wing is assumed to be the sole contribution to the aerodynamic heating. Figure 14 in which cross-flow theory has been plotted for angles of attack from 20° to 35° shows that the theory overpredicts the center-line heating in this angle-of-attack range. The discrepancy at $\alpha = 20^\circ$ is about 50 percent, but as angle of attack increases to $\alpha = 35^\circ$, the difference between data and theory has diminished to about 20 percent. The discrepancy between the data and the crossflow theory is not surprising because of the increased complexity of the flow resulting from the nose bluntness which extends about 2 nose diameters back from the nose even at these high angles of attack. For lower swept delta wings crossflow theory shows better agreement with data (e.g., $\Lambda = 70^\circ$ in ref. 5, $\Lambda = 45^\circ$ and $\Lambda = 67.5^\circ$ in ref. 7).

In figure 14, the deviation of the data points at $\alpha = 25^\circ$ and $\alpha = 30^\circ$ near the trailing edge of the 80° swept wing from the main body of the data suggests the onset of transition. The trailing-edge data points at $\alpha = 35^\circ$ for the Mach 9.6 tests (data marked with "x") should be disregarded because they are influenced by the intersection of the body with the shock from the tunnel-wall separation. Separation at this Mach number was also first observed at $\alpha = 30^\circ$ for the 70° swept wing of reference 5.

Stanton number distribution on wings.- The Stanton number distribution normal to the leading edge of the 80° swept wing at angles of attack for Mach numbers 6.8 and 9.6 is presented in figures 15 and 16, respectively. At angles of attack of 0°, 15°, and 30°, the Stanton number distribution over a geometrically similar slab delta wing with a 70° sweep angle (ref. 5) is included for Mach number 9.6 in figure 16. Lees' theory has been adapted for the two-dimensional leading edge and is included in figures 15 and 16 where it is called swept-cylinder theory. An empirical relation is used for the pressure distribution over the leading-edge region. (See appendix, ref. 5). The Fay and Riddell theory provides the two-dimensional stagnation values of the heating parameter. The Mach number normal to the leading edge has been used to determine the local conditions at each angle of attack. Because the normal Mach number is higher for the 70° swept wing than for the 80° swept wing, the swept-cylinder theory is significantly higher for the lower swept configuration. Even with the decreased normal Mach number employed in the swept-cylinder theory for the leading edge of the 80° swept wing, the theory still overpredicts the trend of the heat-transfer data in this region of the more highly swept wing until $\alpha = 20^\circ$ is reached; above this angle-of-attack agreement is good within the scatter of the data. This disagreement at low angles of attack is the result of the influence of the nose bluntness on the flow behavior. In comparison, the swept-cylinder theory more closely predicts the heating trends of the 70° swept wing throughout the angle-of-attack range.

In the low angle-of-attack range the surface flow is complicated and leads to a wide dispersion in the values of the heating parameter. (See figs. 15(a) and 16(a).) Strip theory over the slab portion of the 70° sweep wing at $\alpha = 0^\circ$ does give a rough approximation of the heat transfer. At the intermediate angle-of-attack range ($10^\circ < \alpha < 25^\circ$) strip theory predicts the level of the heating over the slab of both wings satisfactorily. As angle of attack increases further, strip theory underpredicts the data over the 80° sweep wing (figs. 15(c) and 16(g)) because of the effects of spanwise flow. At $\alpha = 0^\circ$ and $\alpha = 15^\circ$, the heating over the slab portion of the 80° swept wing is lower than that over the 70° swept wing. (See figs. 16(a) and 16(d).) This result is again thought to be a consequence of the fact that the leading edge of the 80° swept wing lies in the shadow of the shock coming from the blunt nose. The contribution of the flow over the leading edge to the heating on the flat portion of the 80° swept wing has been reduced because of this phenomenon. At $\alpha = 30^\circ$ (fig. 16(g)) the flow normal to the wing determines the magnitude of the heat transfer. The heat-transfer levels are nearly the same at this angle of attack since the leading edge now has negligible effect on the flow over the surface exposed to the flow.

Definite signs of transition are first seen for the trailing-edge data points of the 80° swept wing at $\alpha = 30^{\circ}$ (fig. 15(c)) for $M_{\infty} = 6.8$ and at $\alpha = 25^{\circ}$ (fig. 16(f)) for $M_{\infty} = 9.6$. At $\alpha = 35^{\circ}$ (fig. 16(h)) the shock from the separated tunnel boundary layer has struck the model, and therefore the higher levels of the heating parameter in this case must be ignored. Transition would probably occur, however, since the lower angles of attack have already produced transition on parts of the 80° sweep wing. Transition on the 70° sweep wing was also first noticed at $\alpha = 30^{\circ}$.

CONCLUDING REMARKS

Results are presented for a study of a slab delta wing with an 80° sweep angle at Mach numbers of 6.8 and 9.6 in air. The wing had cylindrical leading edges, a hemispherical nose of the same radius, and a length of 7.12 nose diameters.

The most striking phenomenon resulting from the tests on this highly swept wing was the strong influence of the nose region in determining the flow behavior over the leading-edge region at low angles of attack. Two results of this apex influence were apparent in the pressure distribution over the leading edge of the 80° swept wing. Whereas an empirical swept-cylinder correlation successfully predicted the pressure distribution over the leading edge of a geometrically similar delta wing with a lower degree of sweep, the same theory greatly overpredicted the pressure level over the leading edge of the 80° swept wing. There was also a characteristic decrease in the pressures down the leading edge of the 80° swept wing in contrast to the nearly constant pressure level in the same region of a lower swept delta wing. The heat-transfer distribution over the leading-edge region of the 80° swept wing was similarly influenced by the nose region. As angle of attack increased, the nose influence diminished and the heat-transfer and pressure distributions over the leading edge of the 80° swept wing conformed to the two-dimensional swept-cylinder behavior exhibited by the lower swept wings at all angles of attack.

Constant-pressure strip theory predicts the heat transfer correctly over the slab portion of the delta wing only for the intermediate angles of attack. At low angles of attack, the flow is not chordwise and thus does not meet the criteria for strip theory. At the highest angles of attack, the flow turned outward over the slab, and crossflow theory gave the approximate level of the heating in the center-line region.

Transition appears to occur on the trailing edge of the wing at the highest angles of attack. The heat-transfer values in the transition region are twice the experimental laminar-flow values.

Langley Research Center,
National Aeronautics and Space Administration,
Langley Station, Hampton, Va., November 9, 1964.

REFERENCES

1. Eggers, Alfred J., Jr.; Allen, H. Julian; and Neice, Stanford E.: A Comparative Analysis of the Performance of Long-Range Hypervelocity Vehicles. NACA Rep. 1382, 1958. (Supersedes NACA TN 4046.)

2. Penland, Jim A.: Aerodynamic Characteristics of a Circular Cylinder at Mach Number 6.86 and Angles of Attack up to 90°. NACA TN 3861, 1957. (Supersedes NACA RM L54A14.)

3. Bogdonoff, S. M.; and Vas, I. E.: Hypersonic Studies of Blunt Two-Dimensional Swept Wings at Zero Angle of Attack. Rept. 451 (ARL Tech. Note 60-125), Dept. Aeron. Eng., Princeton Univ., Apr. 1959.

4. Dunavant, James C.: Investigation of Heat Transfer and Pressures on Highly Swept Flat and Dihedraled Delta Wings at Mach Numbers of 6.8 and 9.6 and Angles of Attack to 90°. NASA TM X-688, 1962.

5. Bertram, Mitchel H.; and Everhart, Philip E.: An Experimental Study of the Pressure and Heat-Transfer Distribution on a 70° Sweep Slab Delta Wing in Hypersonic Flow. NASA TR R-153, 1963.

6. Bertram, Mitchel H.; and Henderson, Arthur, Jr.: Recent Hypersonic Studies of Wings and Bodies. ARS Jour., vol. 31, no. 8, Aug. 1961, pp. 1129-1139.

7. Paulsen, J. J.: Hypersonic Research Wing - A Study of the Pressure and Heat Transfer Distribution on Highly Swept Slab Delta Wings in Hypersonic Flow. ERR-AN-293, Gen. Dyn./Astronaut., Dec. 1963.

8. Stallings, Robert L., Jr.; Burbank, Paige B.; and Howell, Dorothy T.: Heat-Transfer and Pressure Measurements on Delta Wings at Mach Numbers of 3.51 and 4.65 and Angles of Attack From -45° to 45°. NASA TN D-2387, 1964.

9. Samet, S.; and Isenberg, J. S.: An Experimental Investigation of Hypersonic Aerodynamic Heating on Highly Swept Delta Wing Configurations. ASD-TDR-62-798, U.S. Air Force, Mar. 1963.

10. McLellan, Charles H.; Williams, Thomas W.; and Bertram, Mitchel H.: Investigation of a Two-Step Nozzle in the Langley 11-Inch Hypersonic Tunnel. NACA TN 2171, 1950.

11. Bertram, Mitchel H.: Exploratory Investigation of Boundary-Layer Transition on a Hollow Cylinder at a Mach Number of 6.9. NACA Rep. 1313, 1957. (Supersedes NACA TN 3546.)

12. Bertram, Mitchel H.: Boundary-Layer Displacement Effects in Air at Mach Numbers of 6.8 and 9.6. NASA TR R-22, 1959. (Supersedes NACA TN 4133.)

13. Crawford, Davis H.; and McCauley, William D.: Investigation of the Laminar Aerodynamic Heat-Transfer Characteristics of a Hemisphere-Cylinder in the Langley 11-Inch Hypersonic Tunnel at a Mach Number of 6.8. NACA Rep. 1323, 1957. (Supersedes NACA TN 3706.)

14. Bertram, Mitchel H.; and Feller, William V.: A Simple Method for Determining Heat Transfer, Skin Friction, and Boundary-Layer Thickness for Hypersonic Laminar Boundary-Layer Flows in a Pressure Gradient. NASA MEMO 5-24-59L, 1959.

15. Creager, Marcus O.: An Approximate Method for Calculating Surface Pressures on Curved Profile Blunt Plates in Hypersonic Flow. NASA TN D-71, 1959.

16. Fay, J. A.; and Riddell, F. R.: Theory of Stagnation Point Heat Transfer in Dissociated Air. Jour. Aero. Sci., vol. 25, no. 2, Feb. 1958, pp. 73-85, 121.

17. Lees, Lester: Laminar Heat Transfer Over Blunt-Nosed Bodies at Hypersonic Flight Speeds. Jet Propulsion, vol. 26, no. 4, Apr. 1956, pp. 259-269, 274.

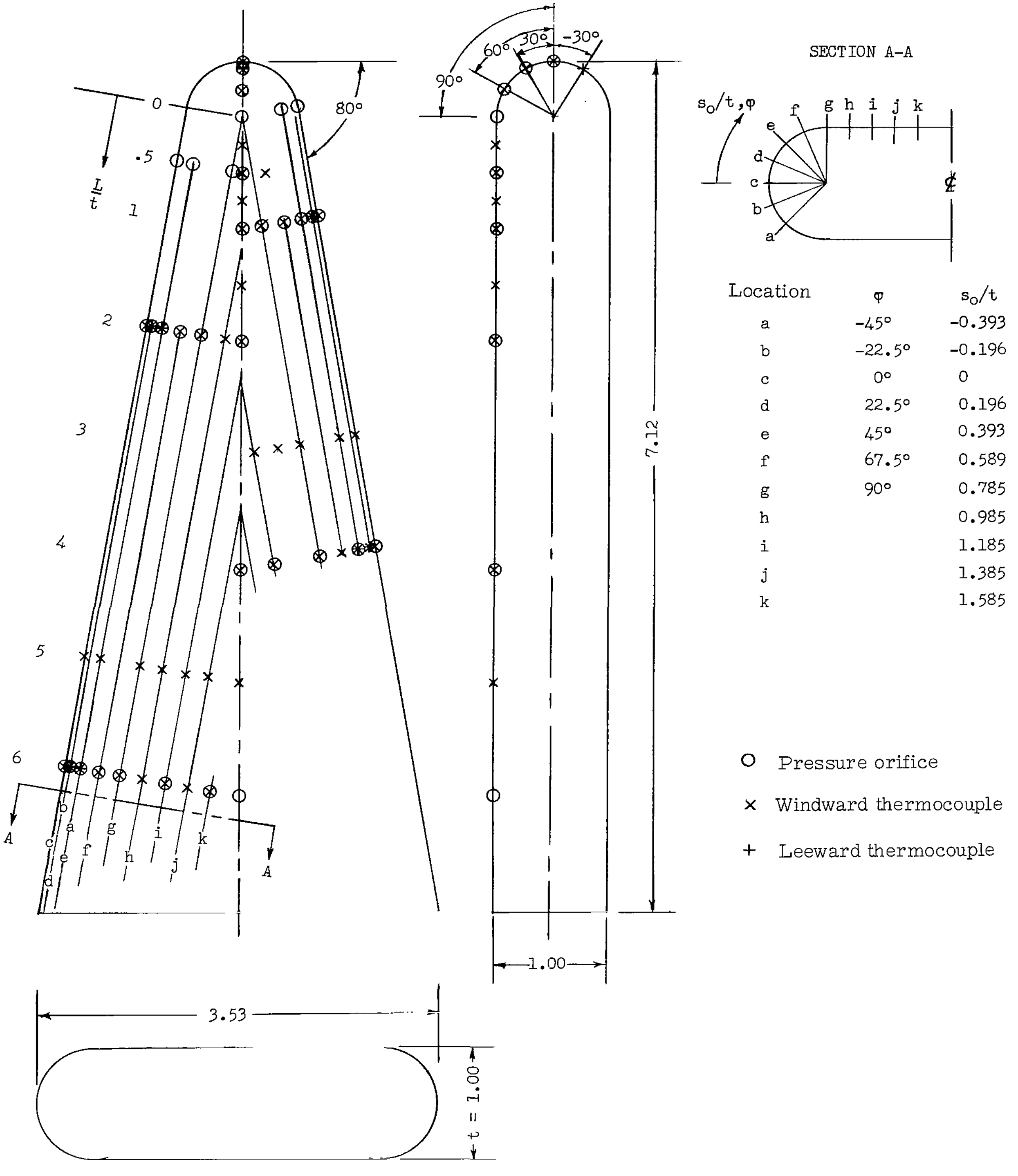

Location	φ	s_o/t
a	-45°	-0.393
b	-22.5°	-0.196
c	0°	0
d	22.5°	0.196
e	45°	0.393
f	67.5°	0.589
g	90°	0.785
h		0.985
i		1.185
j		1.385
k		1.585

Figure 1.- Sketch of pressure and temperature models. All dimensions are in inches except for angle designations.

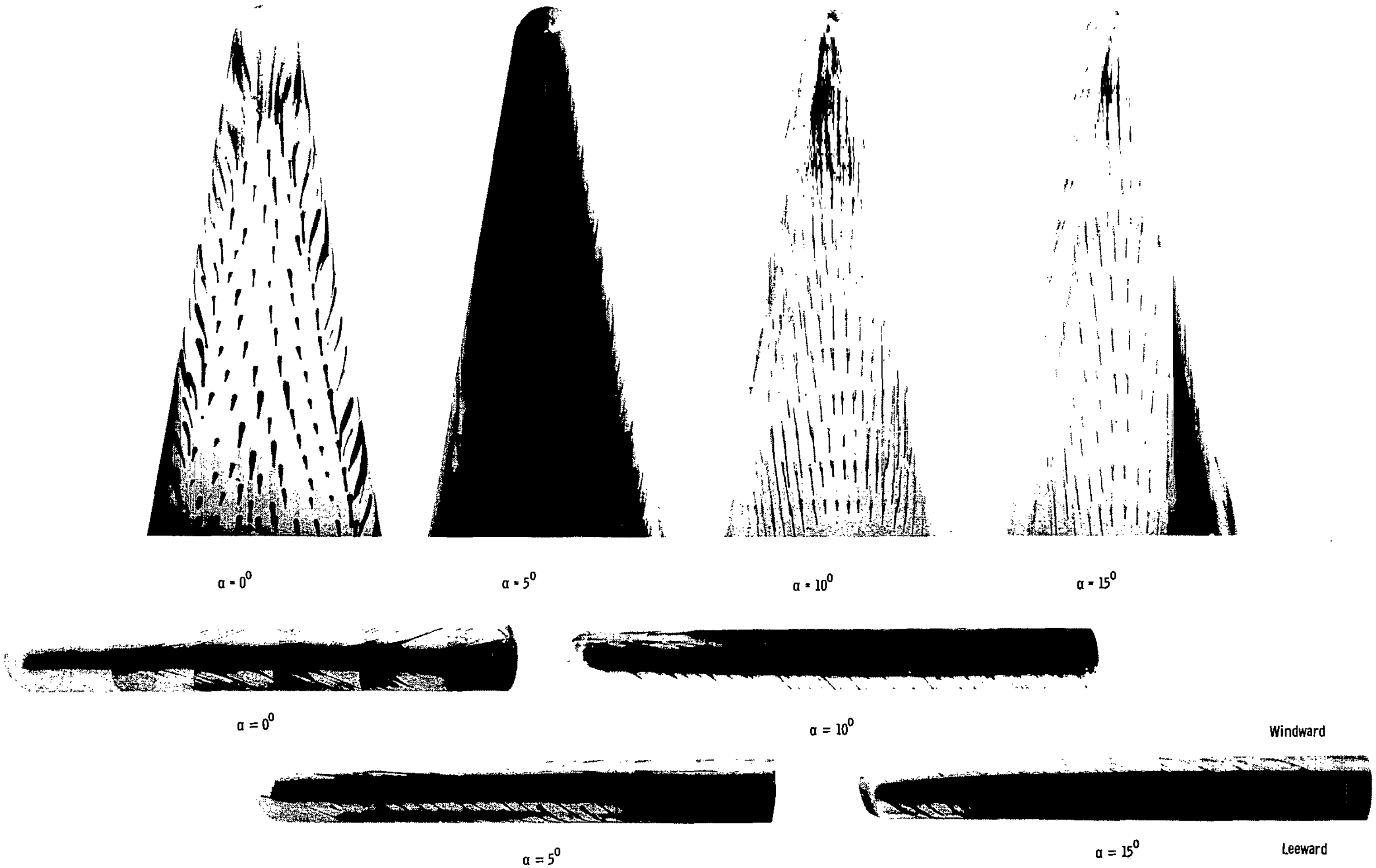

α = 0°

α = 5°

α = 10°

α = 15°

α = 0°

α = 10°

α = 5°

α = 15°

Figure 2.- Surface flow studies at $M_\infty = 6.8$.

L-64-10205

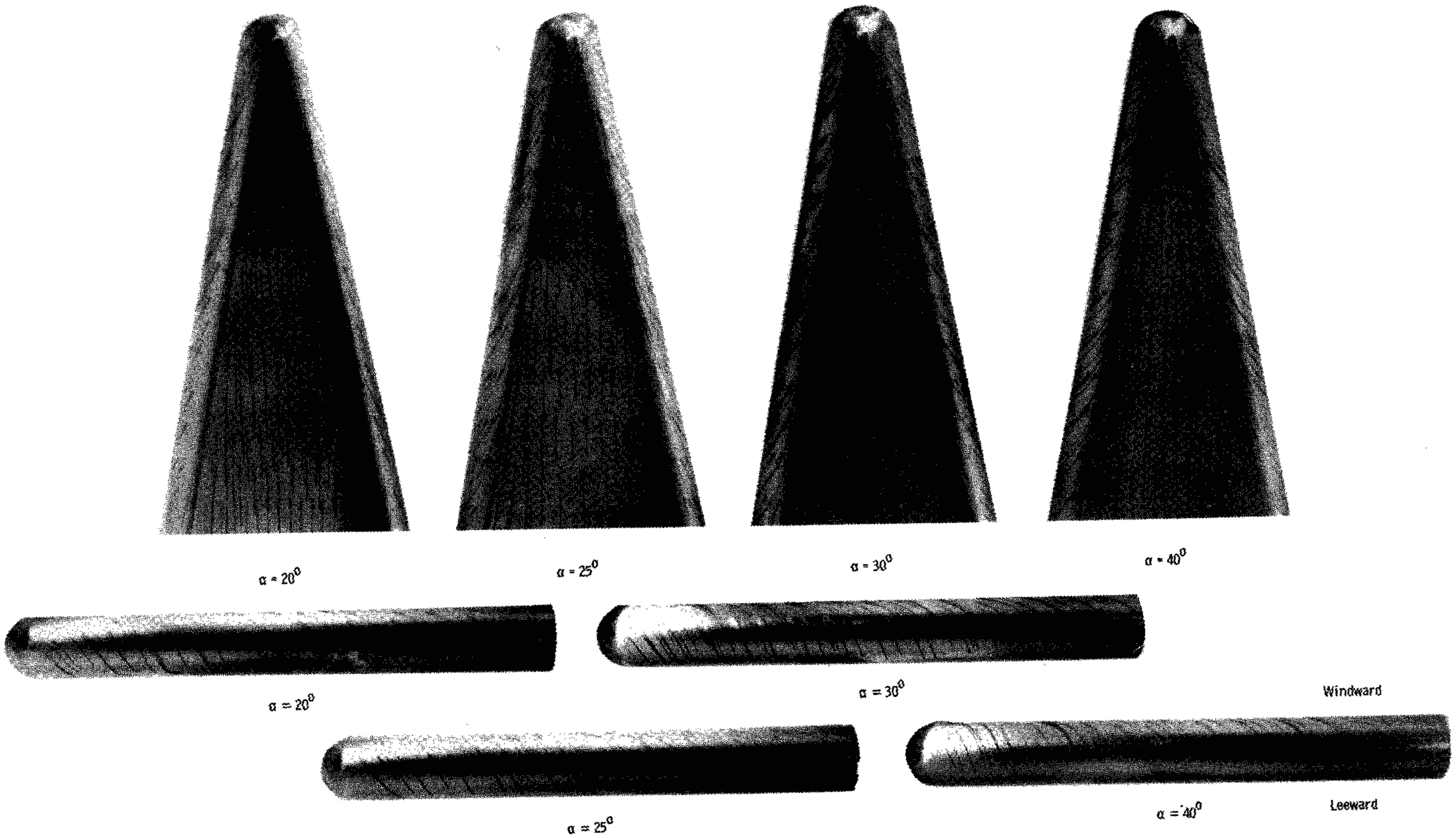

Figure 2.- Concluded.

L-64-10206

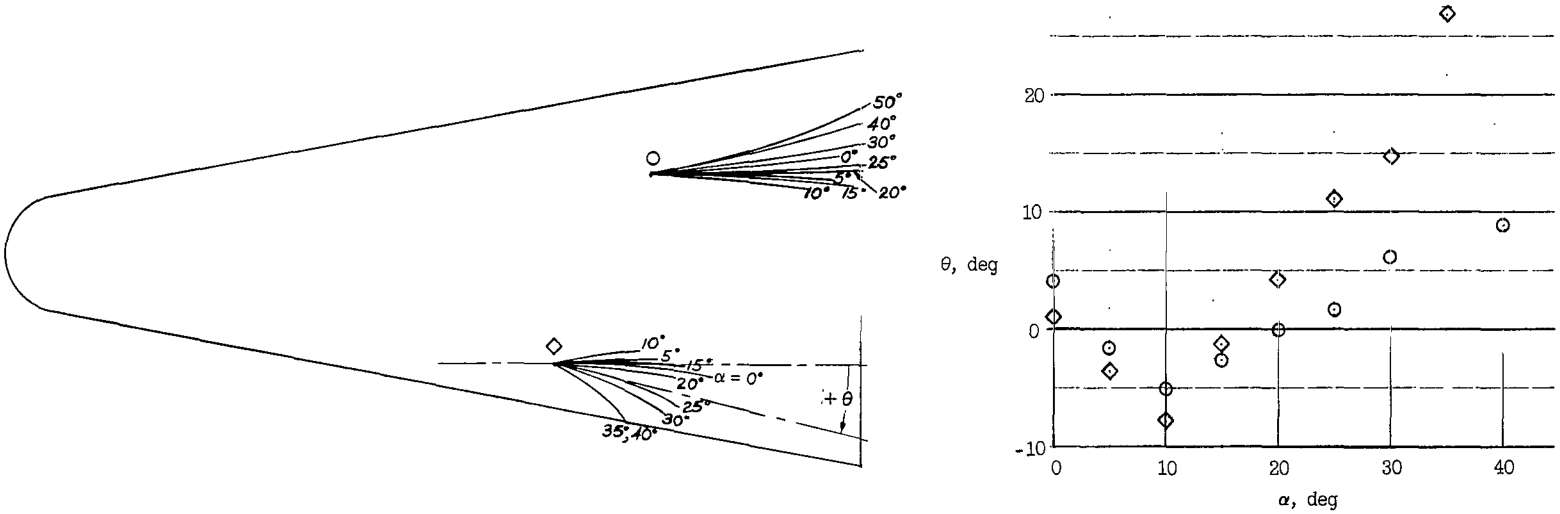

(a) Variation of oil flow on slab with angle of attack.

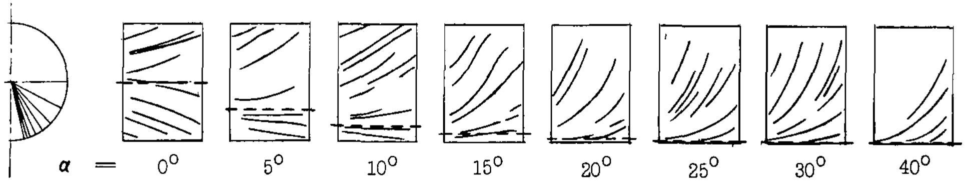

(b) Variation of oil flow on leading edge with angle of attack. Dashed lines indicate theoretical swept-cylinder stagnation lines.

Figure 3.- Composite oil-flow sketch.

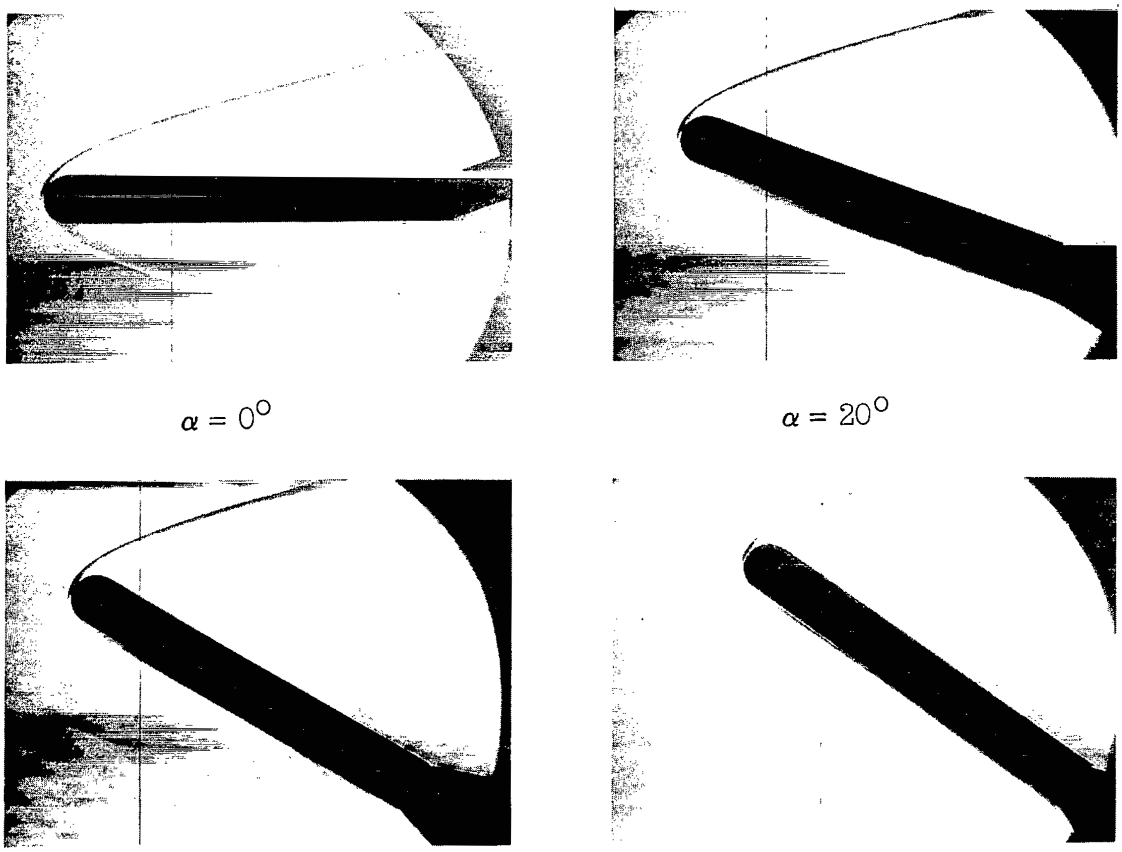

$\alpha = 0^\circ$

$\alpha = 20^\circ$

$\alpha = 30^\circ$

$\alpha = 35^\circ$

(a) $M_\infty = 6.8$; $R_{\infty,t} = 9.9 \times 10^4$. L-64-10207

Figure 4.- Side-view schlieren photographs of 80° swept delta wing.

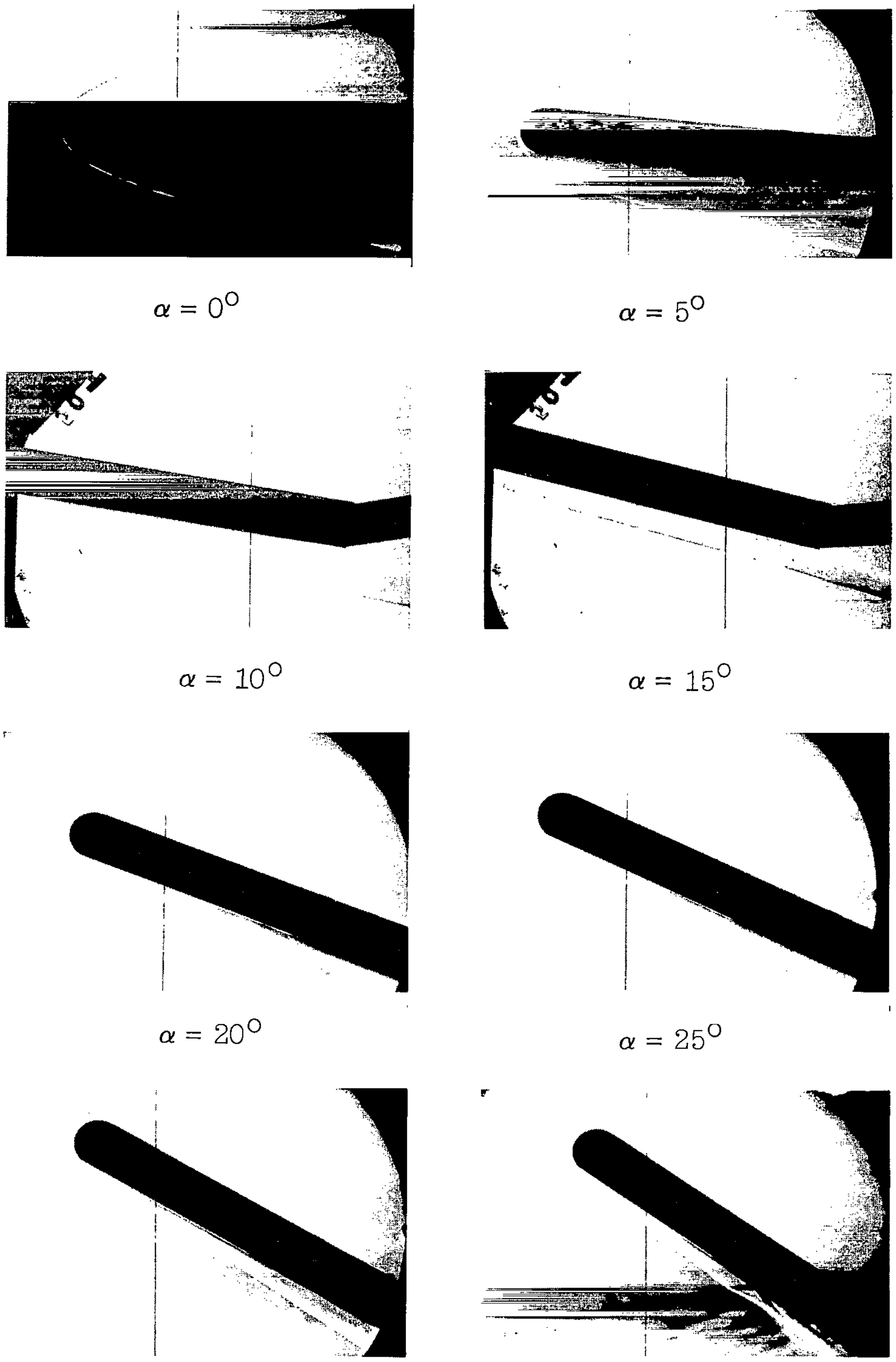

$\alpha = 0^{\circ}$ $\alpha = 5^{\circ}$

$\alpha = 10^{\circ}$ $\alpha = 15^{\circ}$

$\alpha = 20^{\circ}$ $\alpha = 25^{\circ}$

$\alpha = 30^{\circ}$ $\alpha = 35^{\circ}$

(b) $M_{\infty} = 9.6$; $R_{\infty,t} = 10 \times 10^{4}$. L-64-10208

Figure 4.- Concluded.

$\alpha = 0°; \quad \Lambda = 70°$ (ref. 5) $\alpha = 20°; \quad \Lambda = 70°$

$\alpha = 0°; \quad \Lambda = 80°$ $\alpha = 20°; \quad \Lambda = 80°$

$\alpha = 0°; \quad \Lambda = 90°$

L-64-10209

Figure 5.- Top-view schlieren photographs of three highly swept delta wings. $M_\infty = 6.8$.

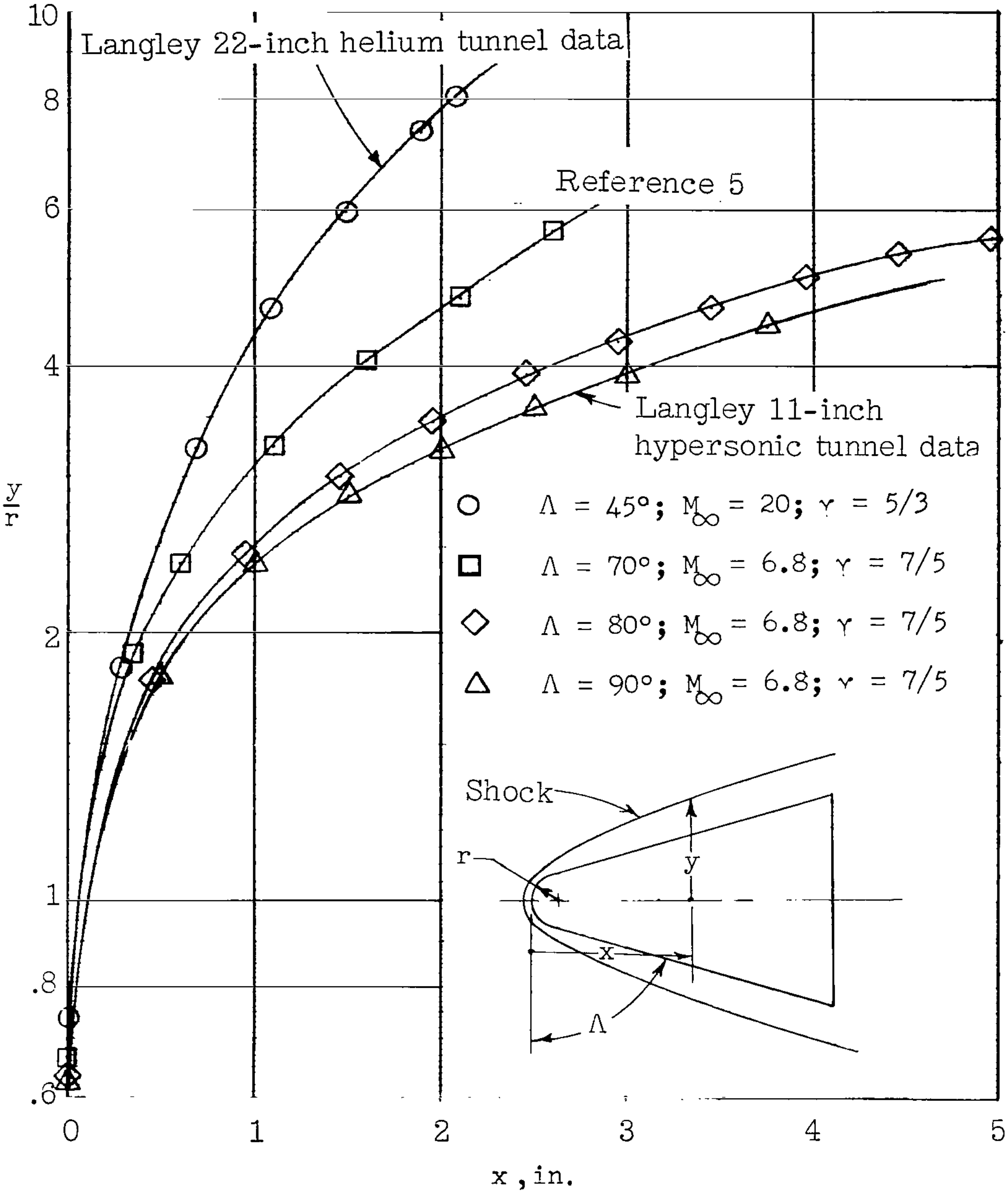

Figure 6.- Leading-edge shock-detachment distance for delta wings with different sweep angles.

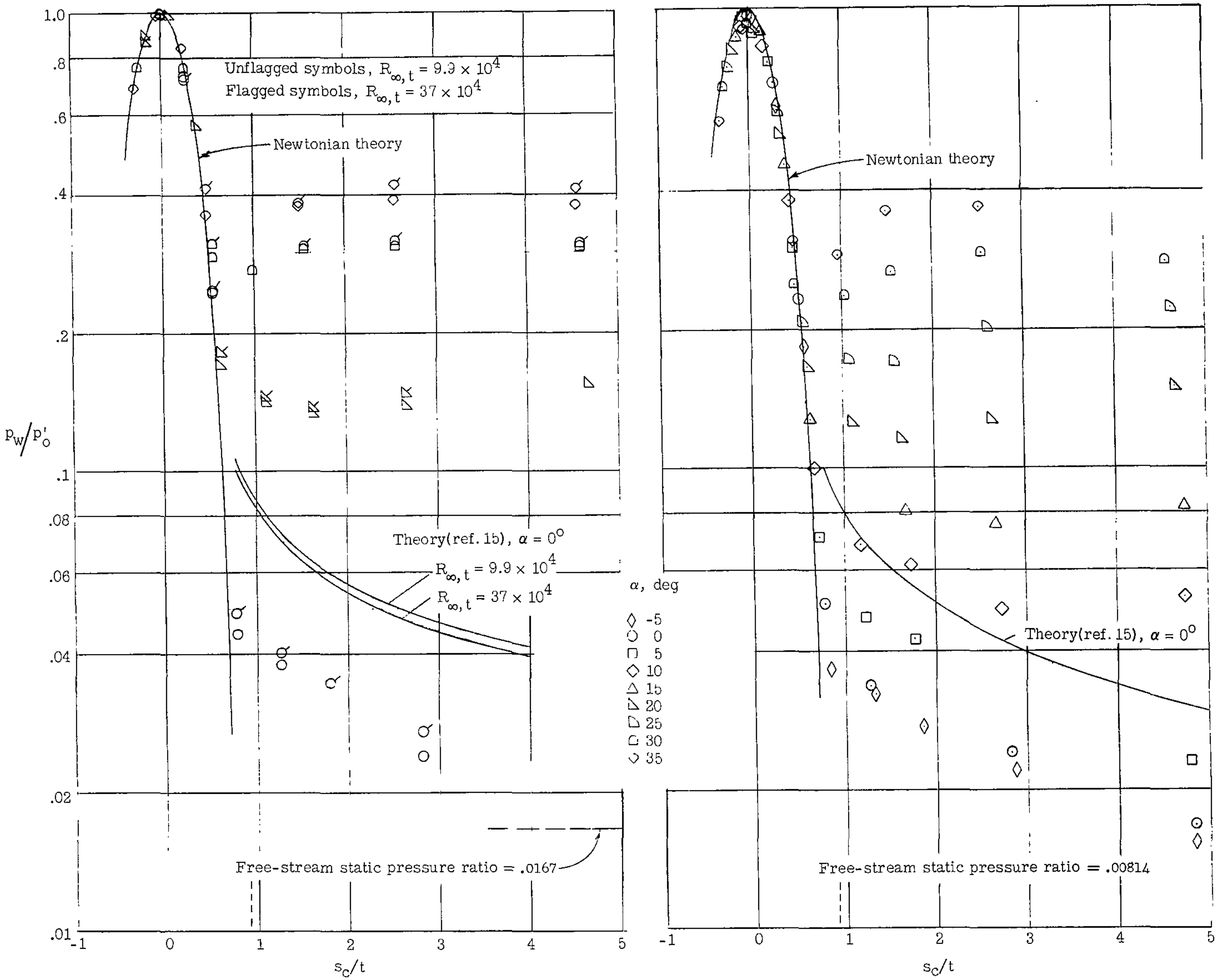

(a) M_∞ = 6.8.

(b) M_∞ = 9.6; $R_{\infty,t}$ = 10 × 10^4.

Figure 7.- Center-line pressure distribution on slab delta wing. Λ = 80°.

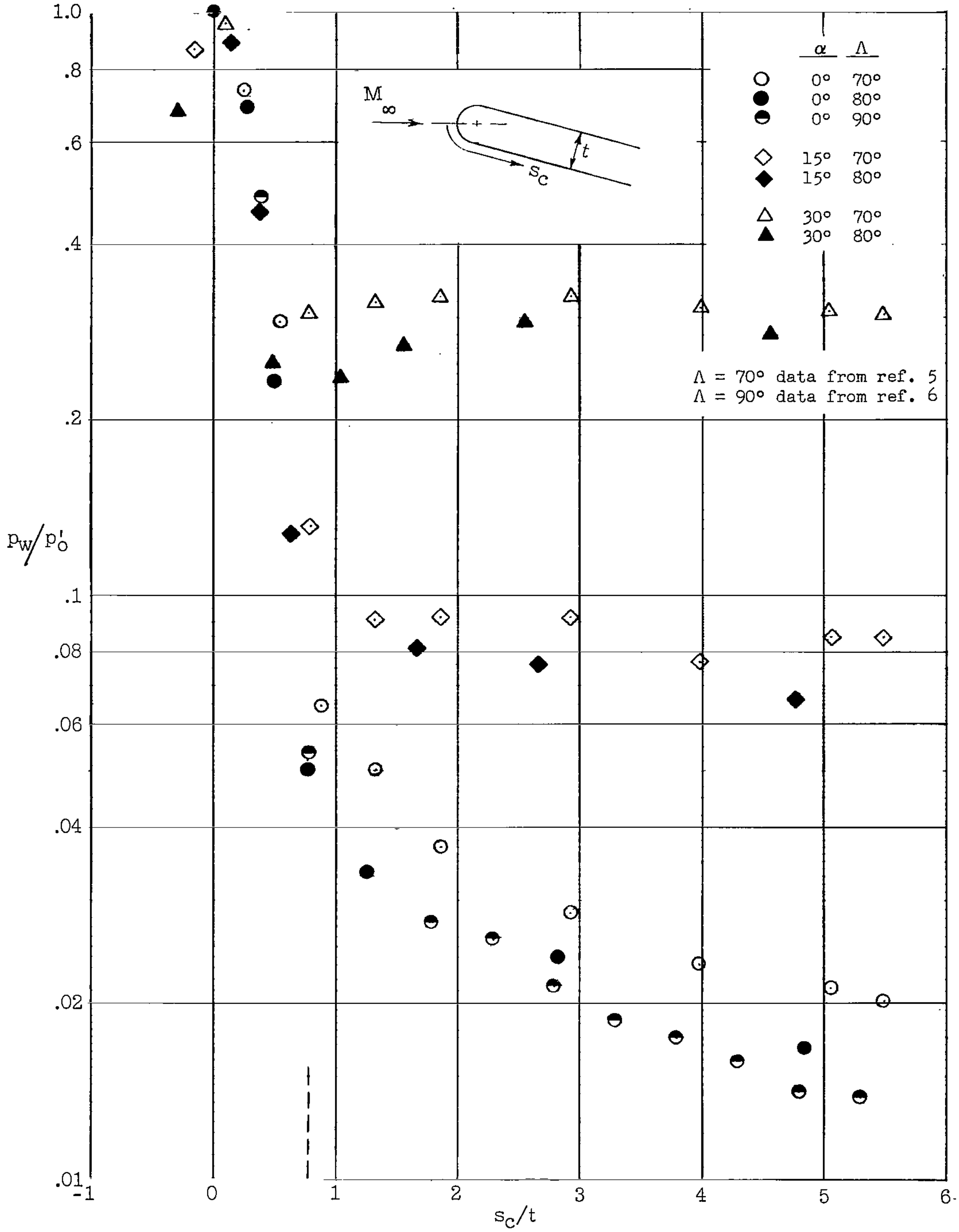

(a) Center-line pressure distribution.

Figure 8.- Pressure distribution over highly swept delta wings. $M_\infty = 9.6$; $R_\infty = 10 \times 10^4$.

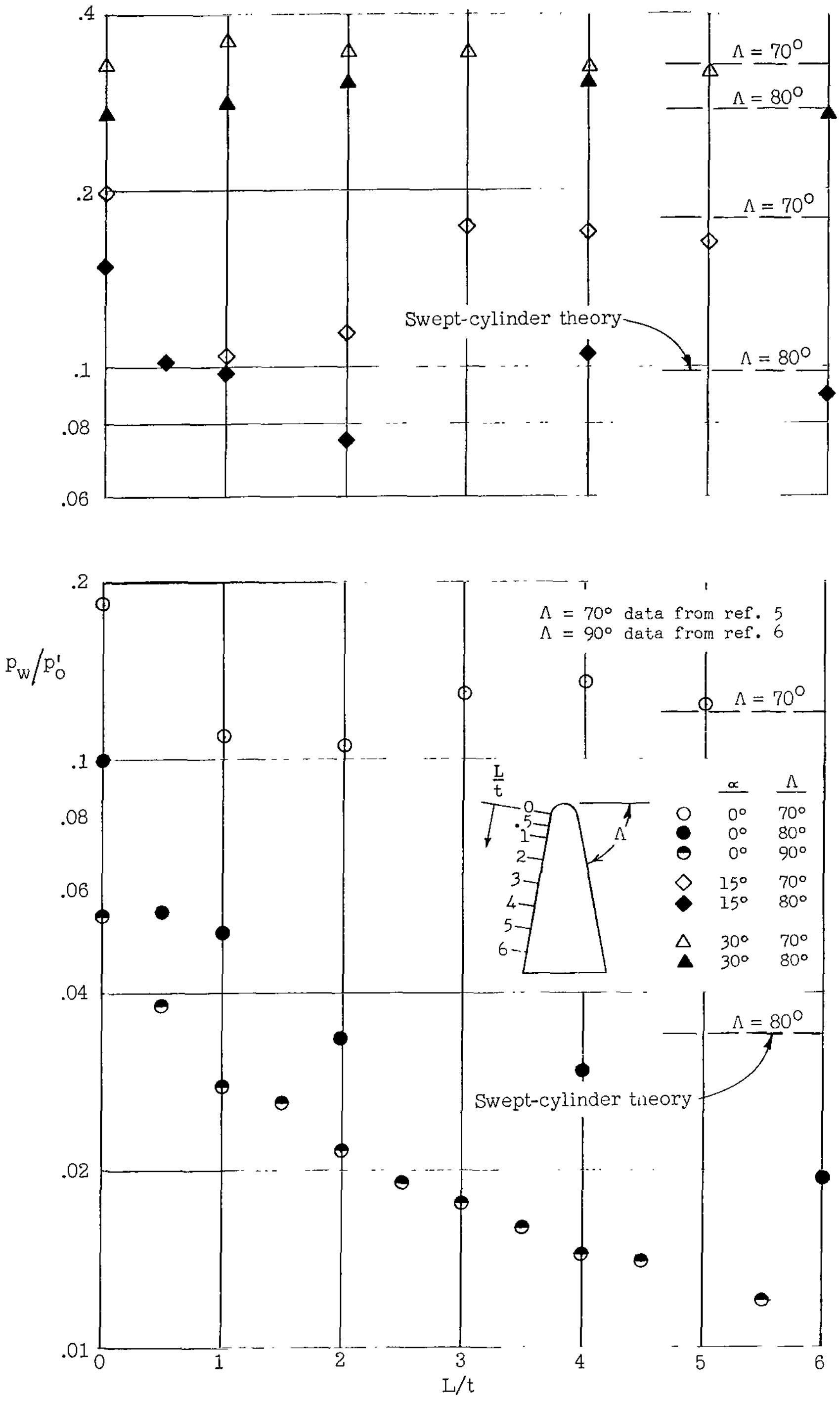

(b) Leading-edge pressure distribution.

Figure 8.- Concluded.

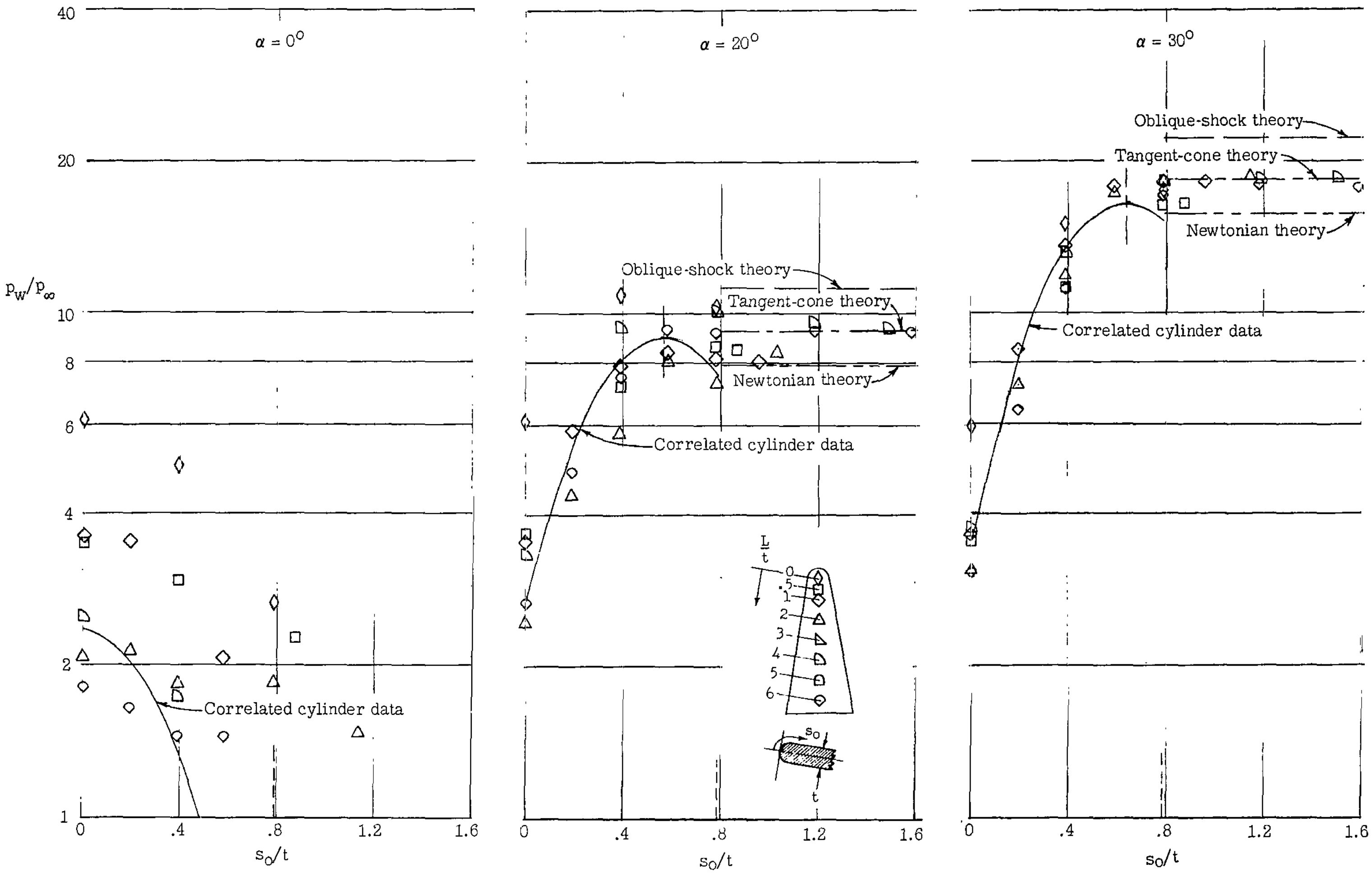

(a) $R_{\infty,t} = 9.9 \times 10^4$.

Figure 9.- Pressure distribution normal to leading edge on 80° swept delta wing at various stations along leading edge for different angles of attack. $M_\infty = 6.8$.

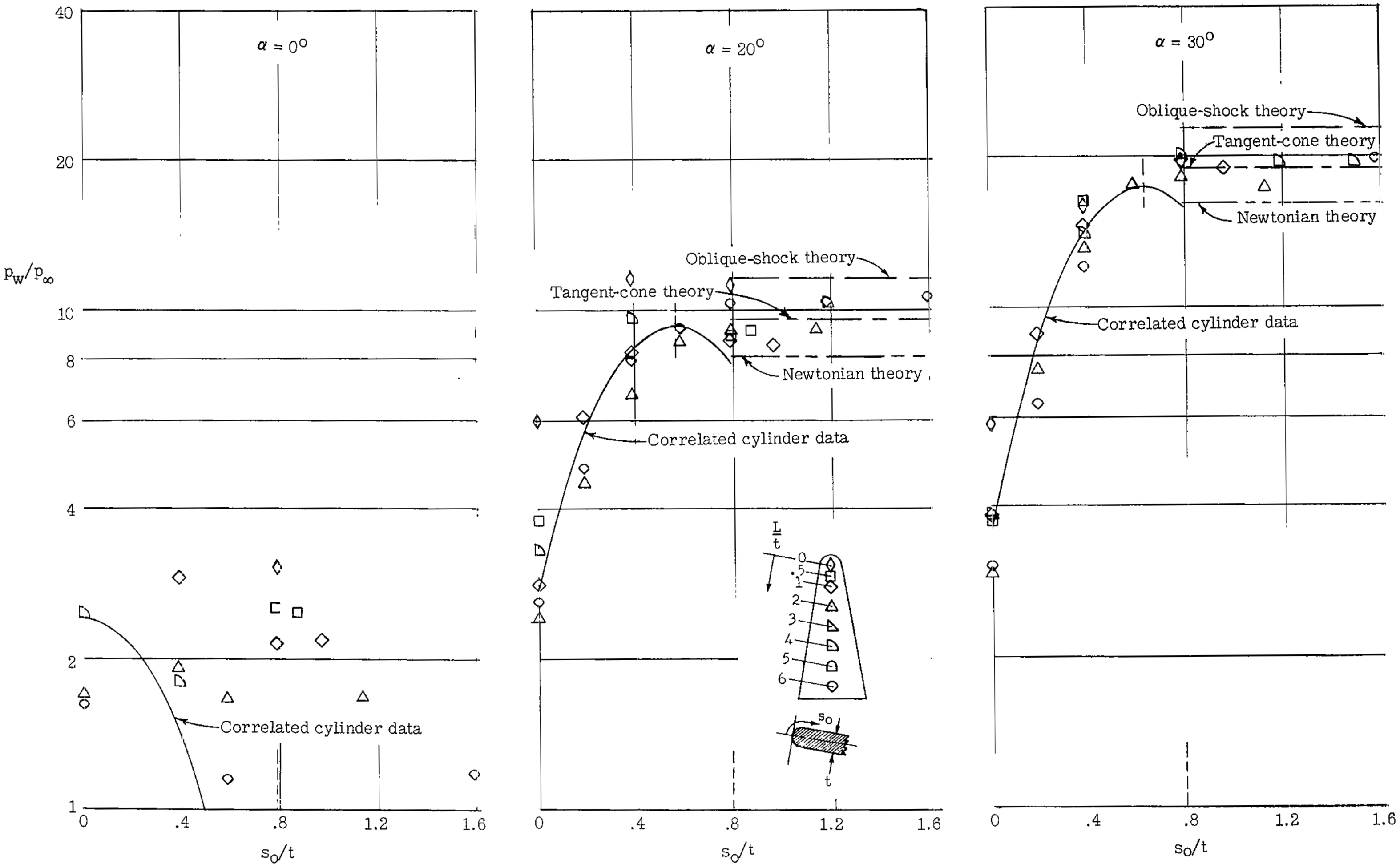

(b) $R_{\infty,t} = 37 \times 10^4$.

Figure 9.- Concluded.

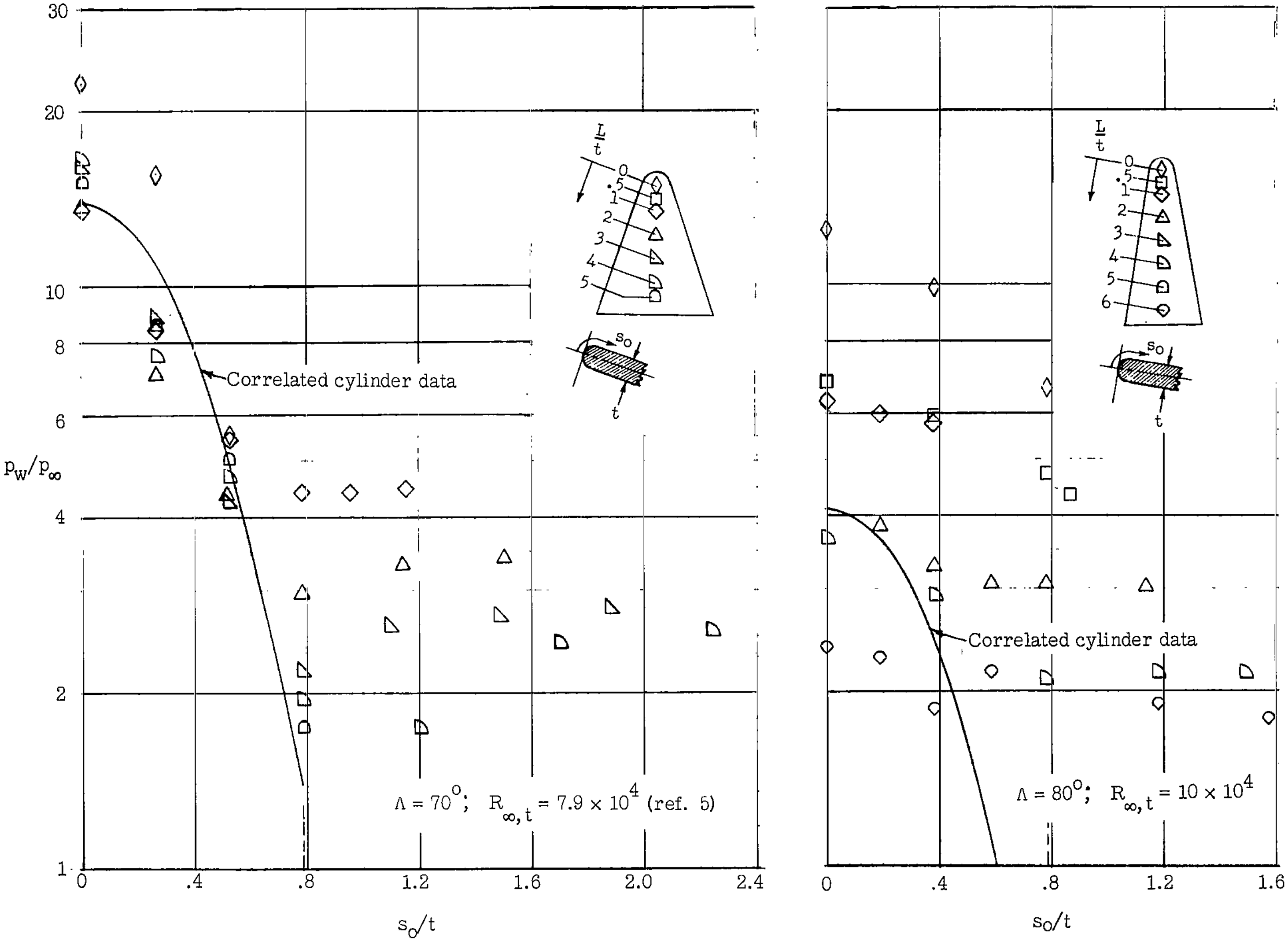

(a) $\alpha = 0^\circ$.

Figure 10.- Pressure distribution normal to leading edge on 70° and 80° swept delta wings at various stations along leading edge for different angles of attack. $M_\infty = 9.6$.

$\Lambda = 80^{\circ}$; $R_{\infty,t} = 10 \times 10^{4}$

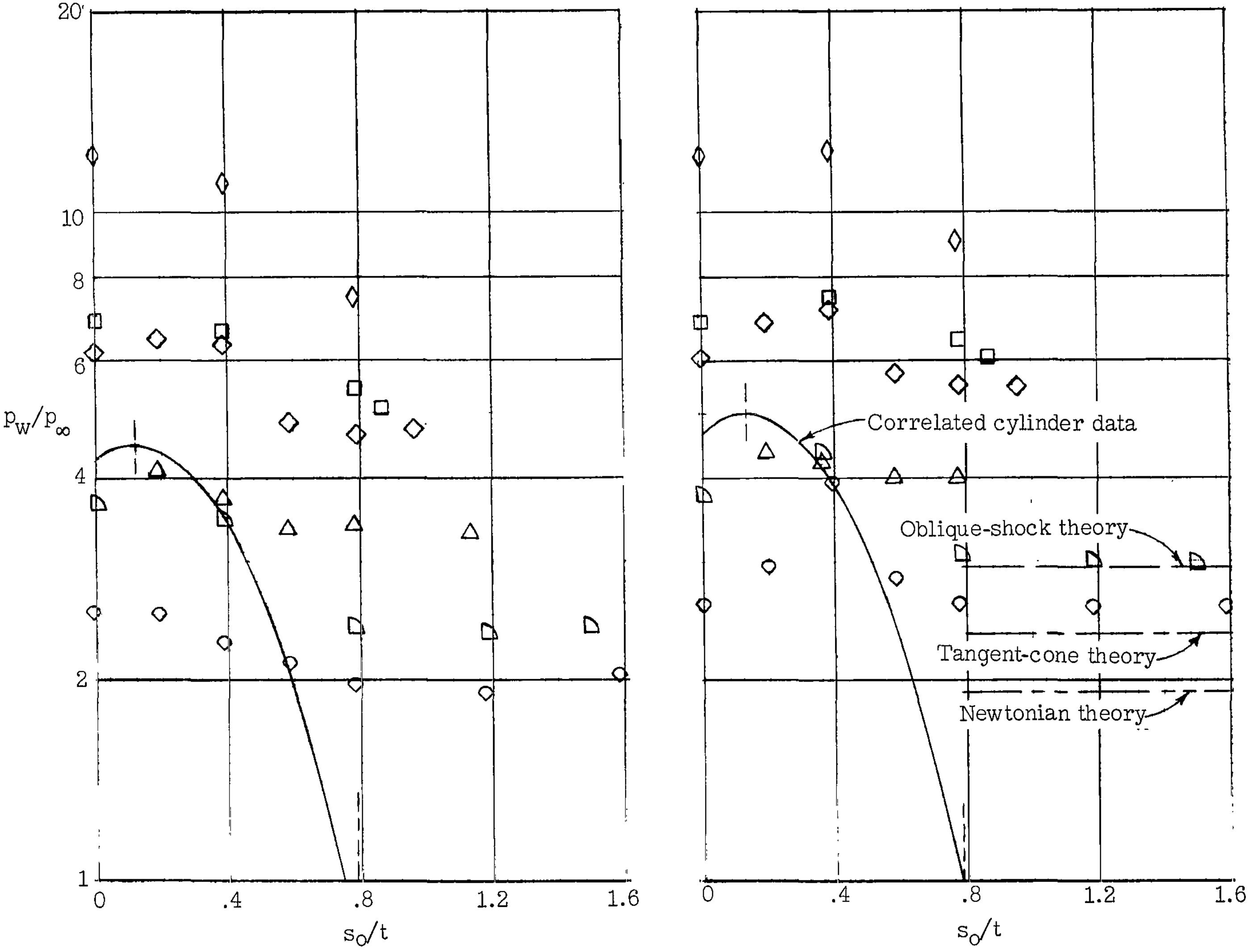

(b) $\alpha = 2\frac{1}{2}^{\circ}$.

(c) $\alpha = 5^{\circ}$.

Figure 10.- Continued.

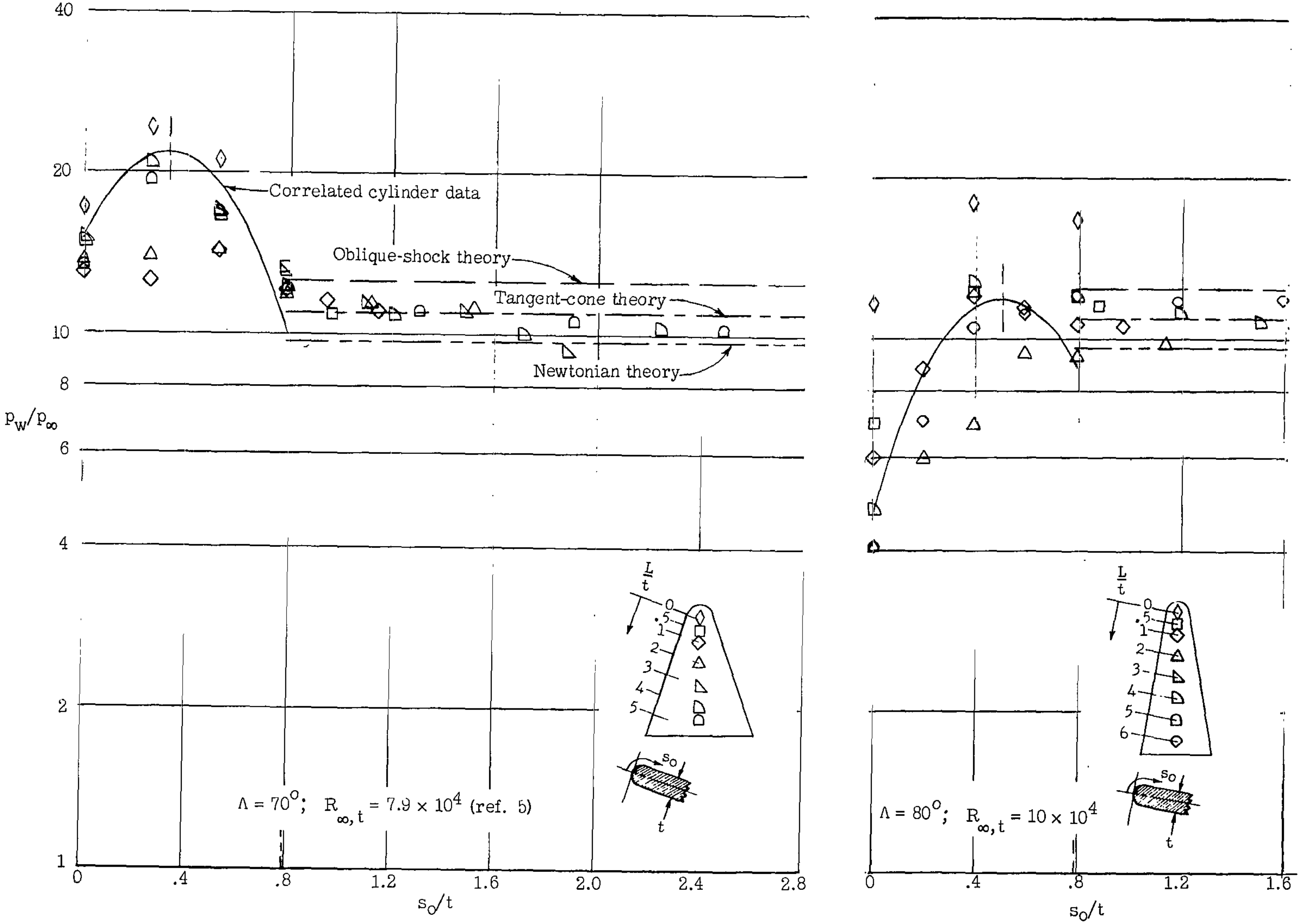

(d) $\alpha = 15^{\circ}$.

Figure 10.- Continued.

$\Lambda = 80^\circ$; $R_{\infty,t} = 10 \times 10^4$

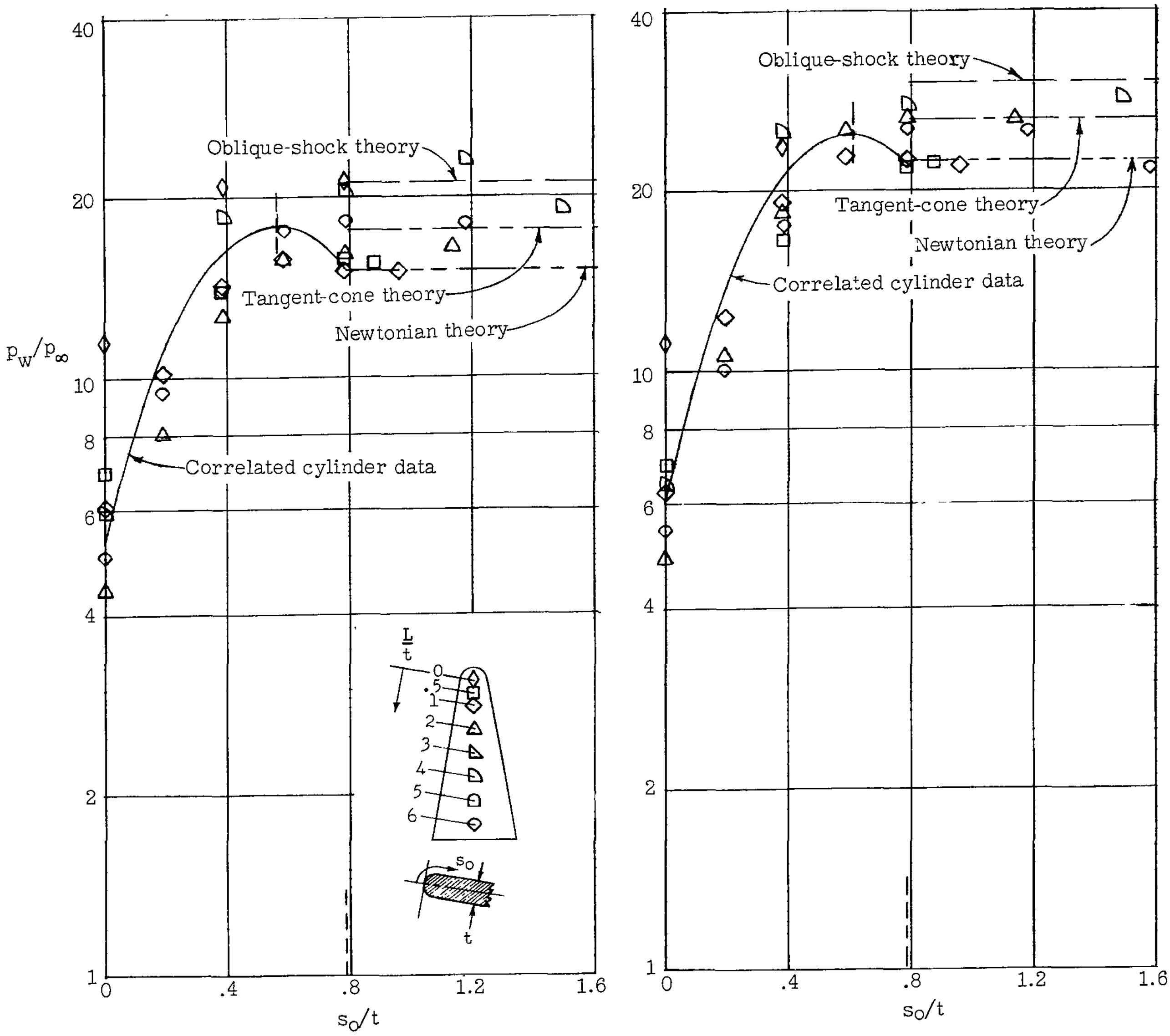

(e) $\alpha = 20^\circ$.

(f) $\alpha = 25^\circ$.

Figure 10.- Continued.

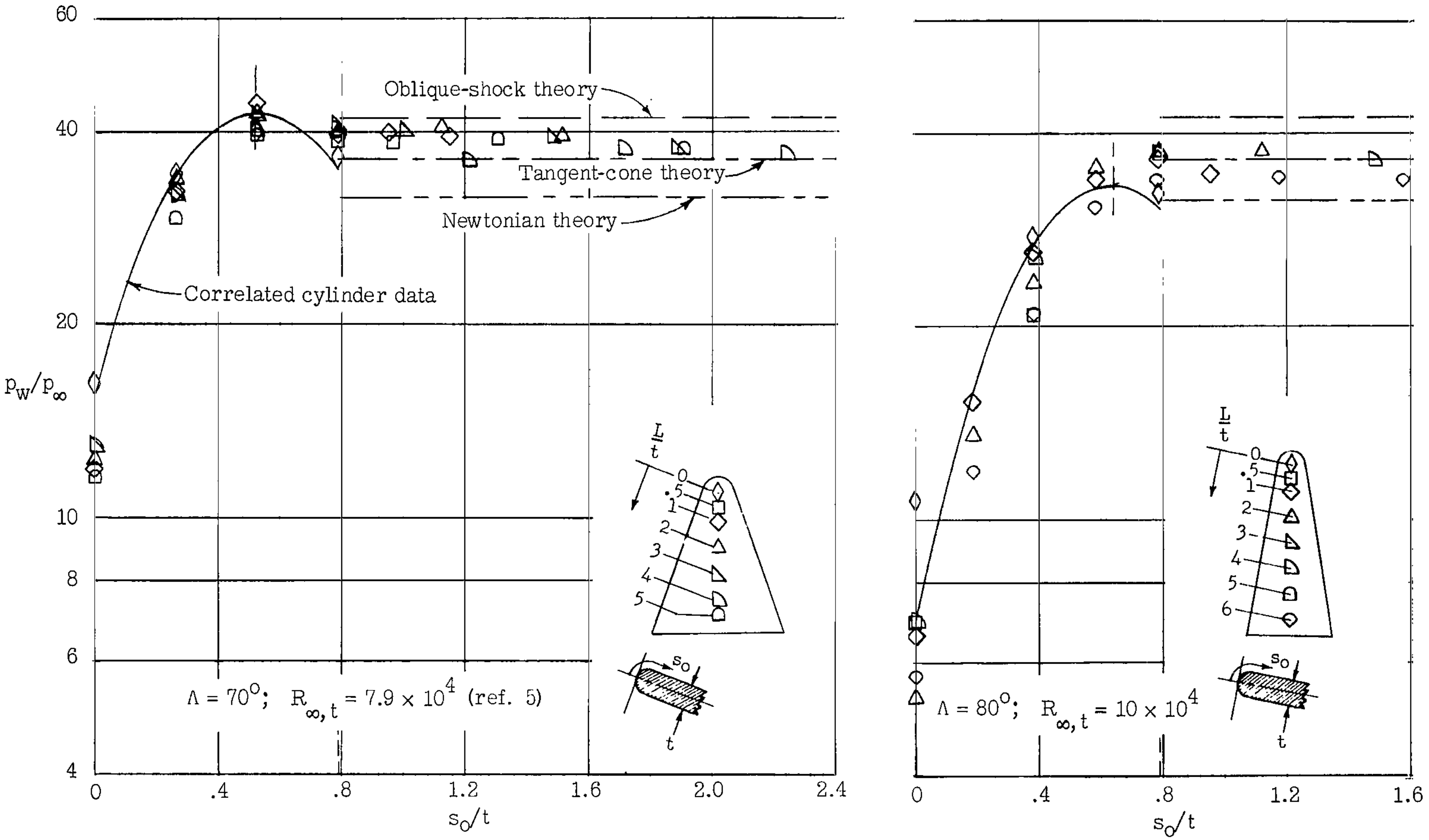

(g) $\alpha = 30^\circ$.

Figure 10.- Continued.

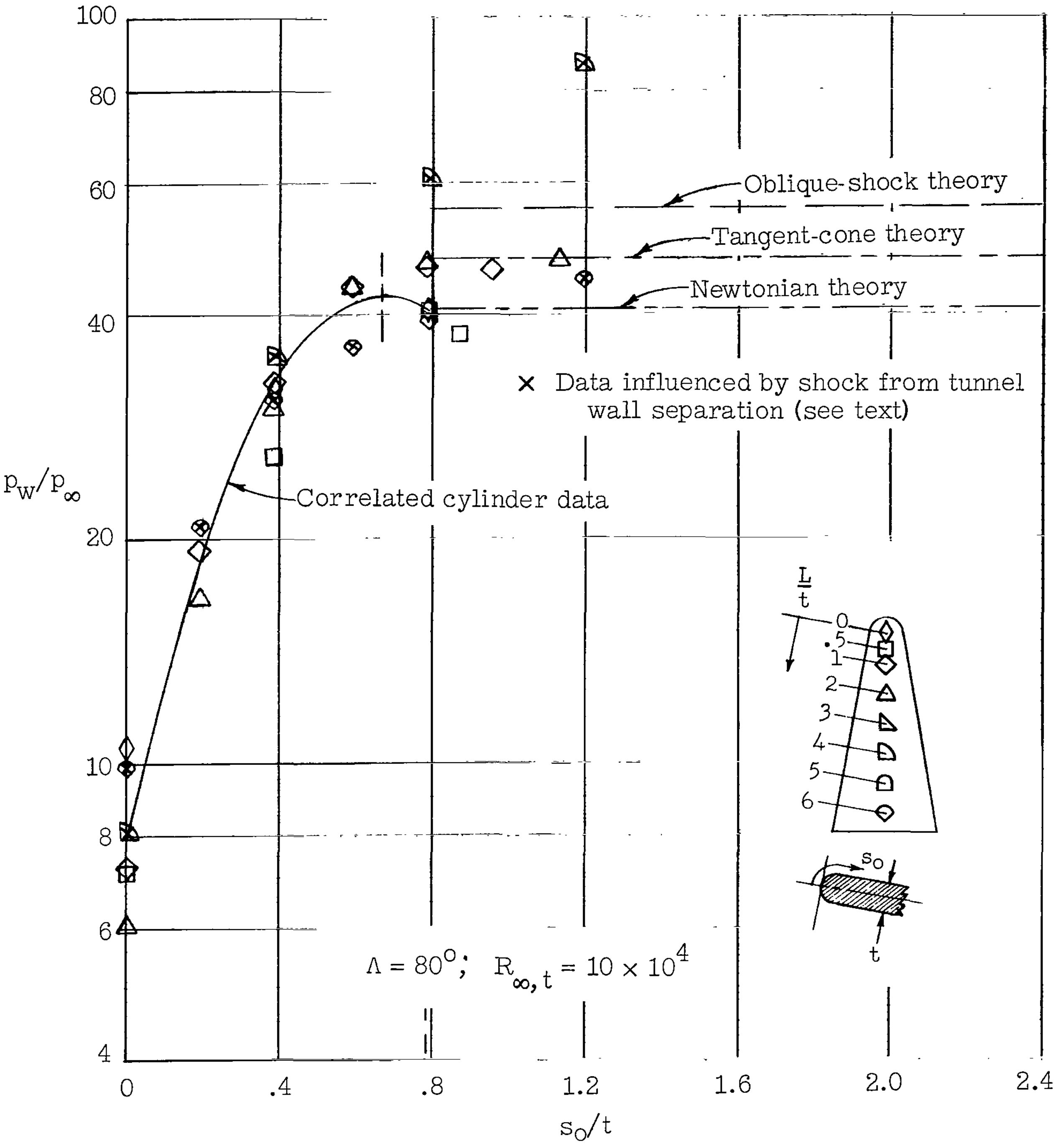

(h) $\alpha = 35^\circ$.

Figure 10.- Concluded.

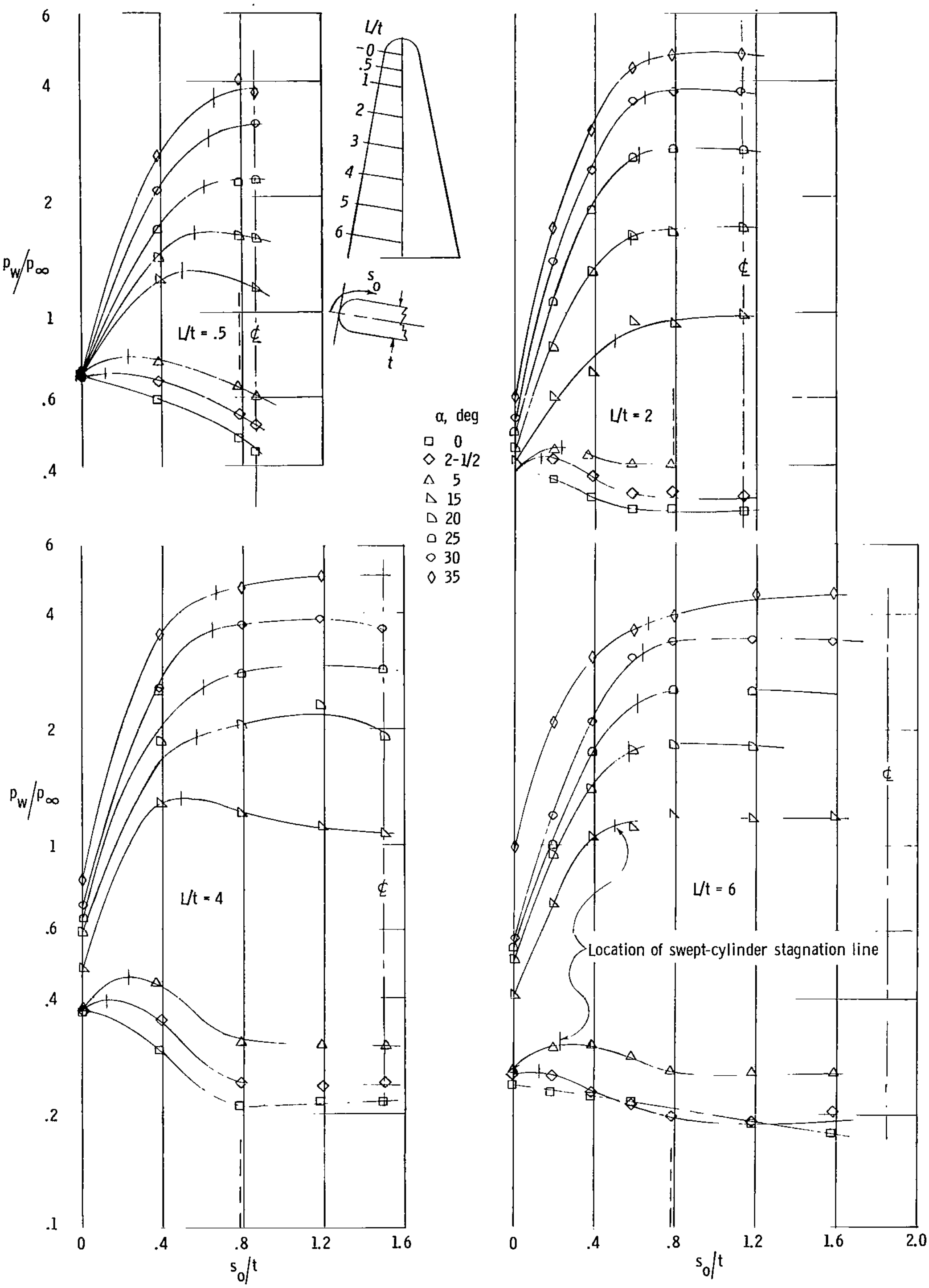

Figure 11.- Pressure distribution normal to leading edge of 80° swept delta wing with angle of attack as parameter. $M_\infty = 9.6$.

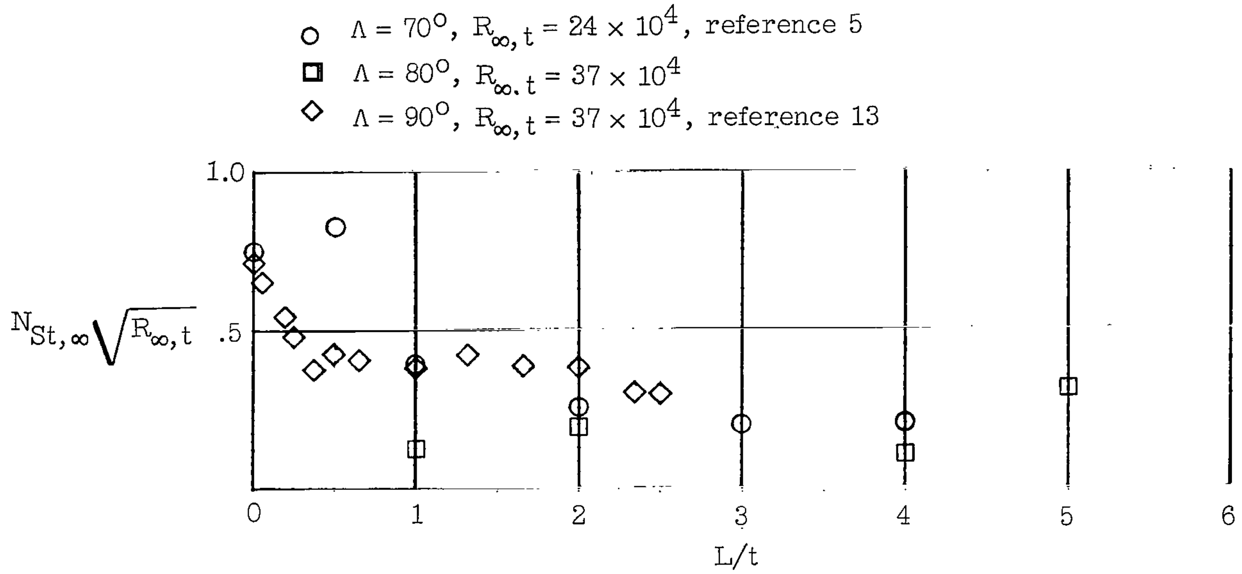

(a) Center-line distribution.

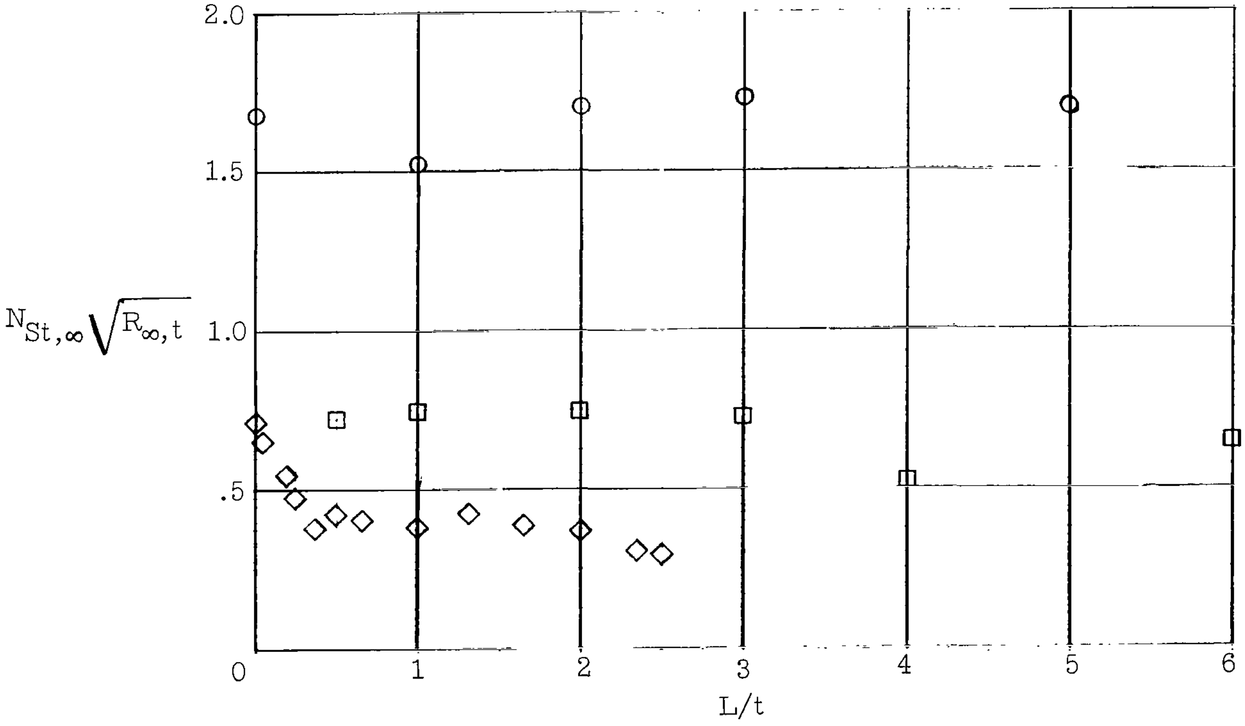

(b) Leading-edge distribution. $s_o/t = 0$.

Figure 12.- Heat-transfer distributions over swept delta wings. $\alpha \approx 0^\circ$ and $M_\infty = 6.8$.

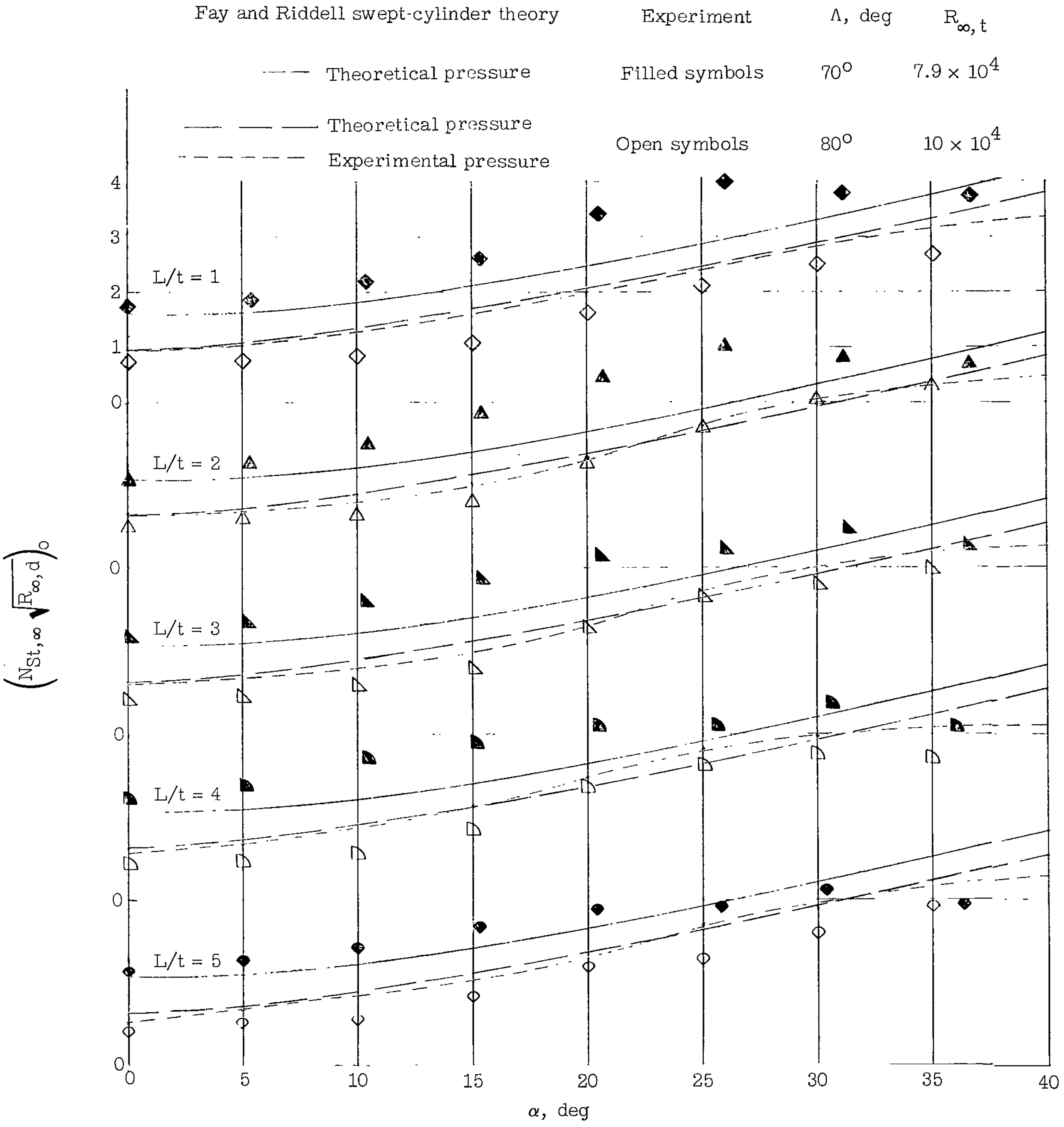

Figure 13.- Maximum Stanton numbers measured at various stations along leading edge of the 70° and 80° swept delta wings. $M_\infty = 9.6$.

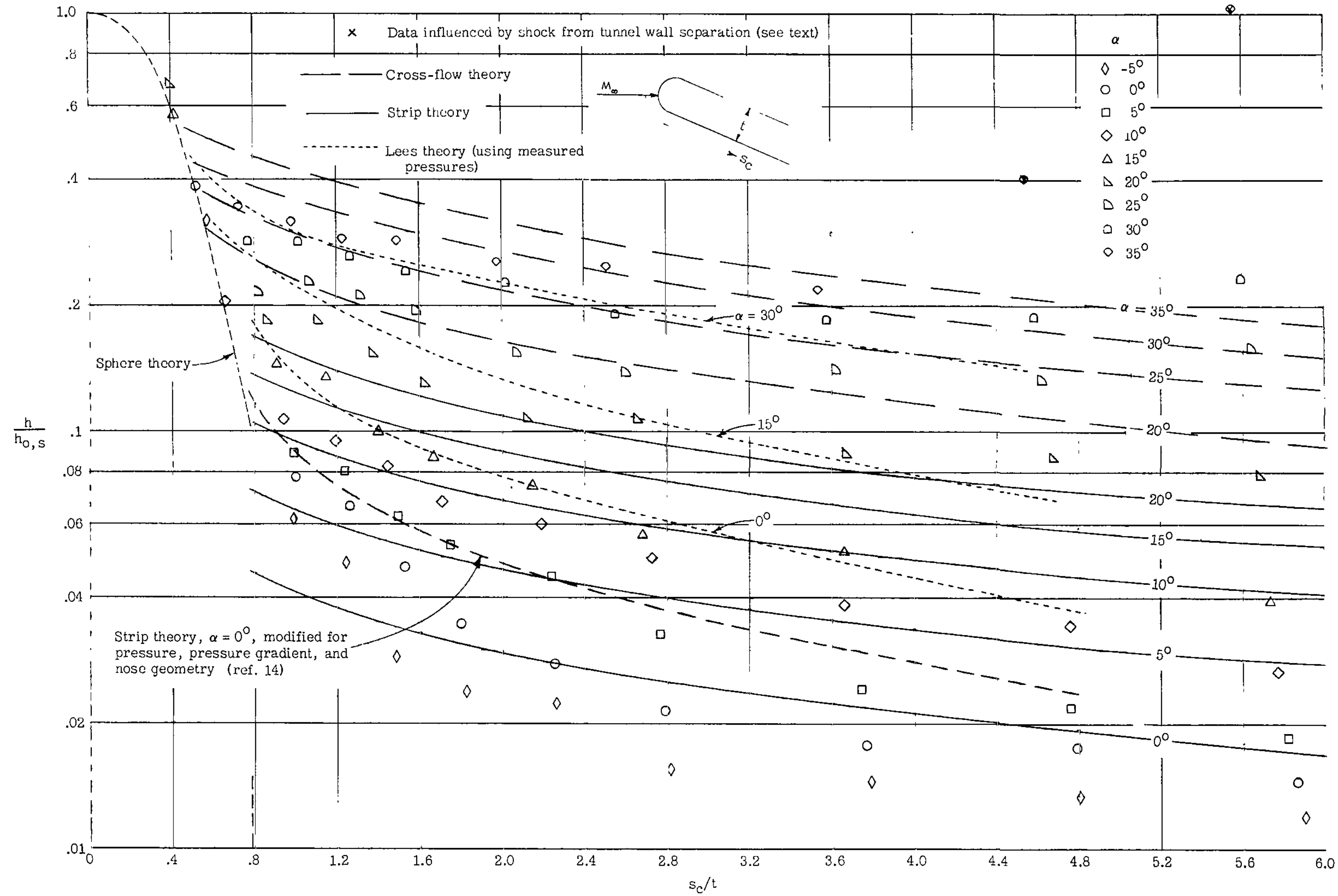

Figure 14.- Center-line distribution of heat-transfer coefficient. $\Lambda = 80°$; $M_\infty = 9.6$.

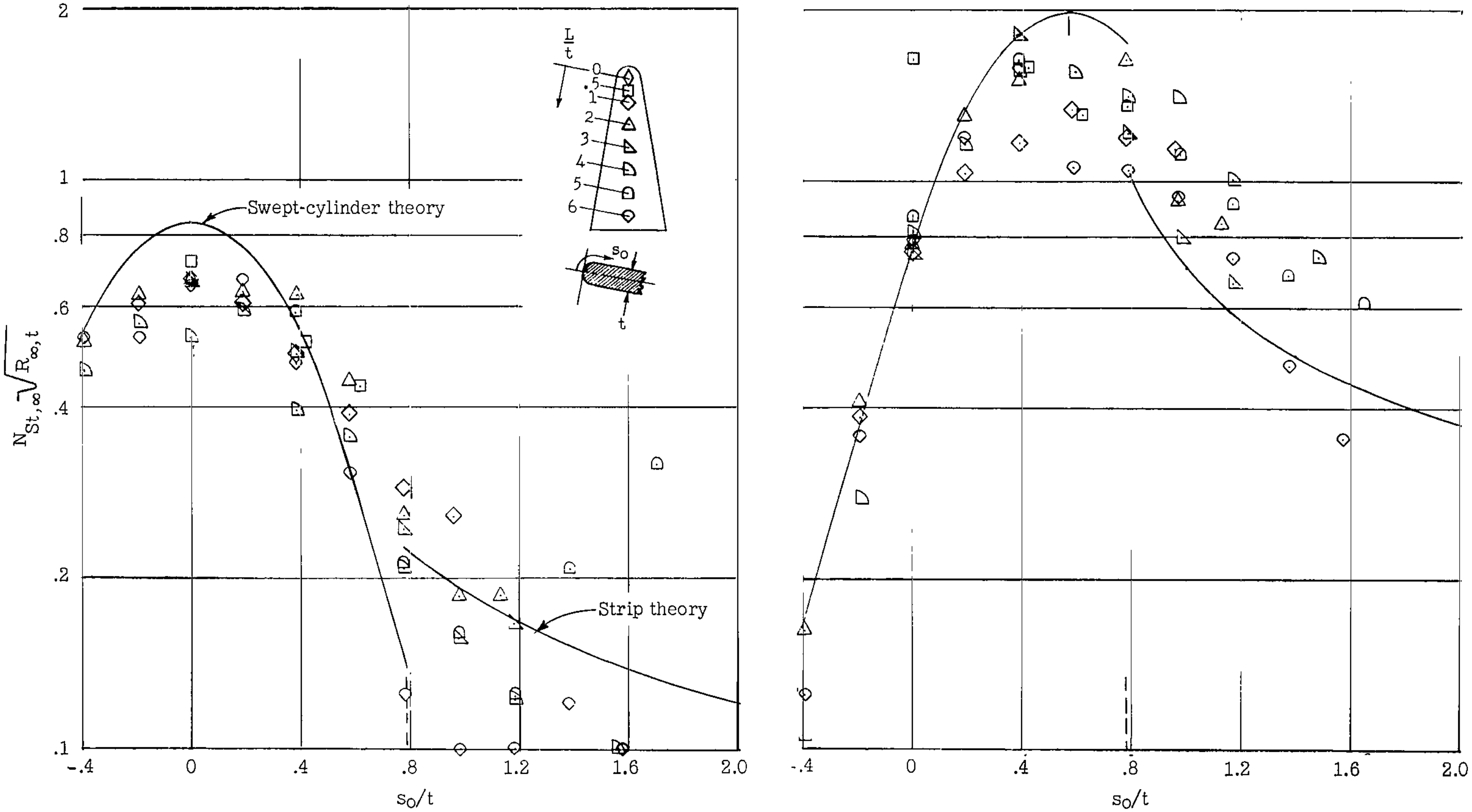

(a) α = 0°.

(b) α = 20°.

Figure 15.- Stanton number distribution normal to leading edge on 80° swept delta wing at various stations along leading edge at different angles of attack. $M_\infty = 6.8$; $R_{\infty,t} = 37 \times 10^4$.

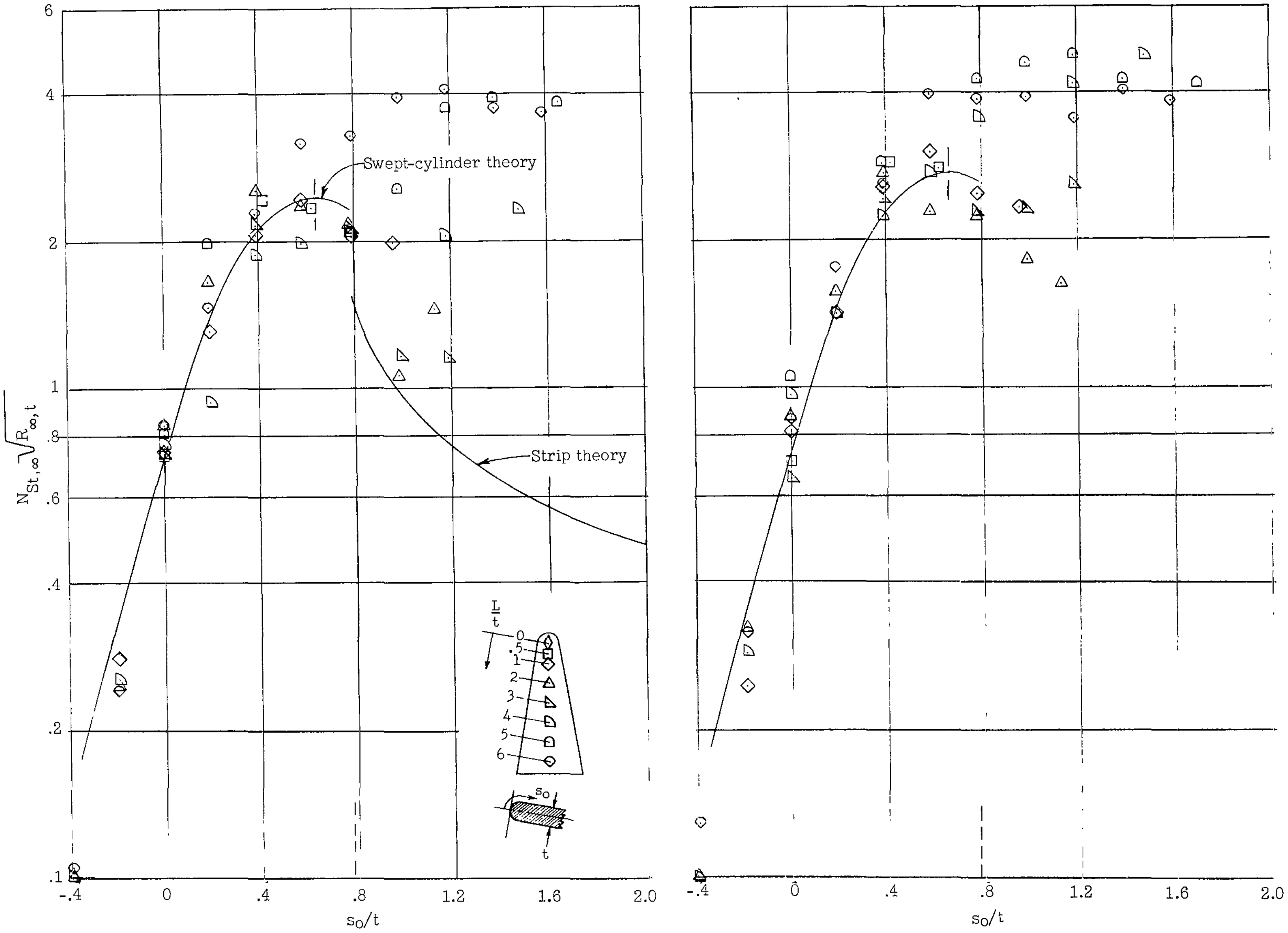

(c) α = 30°.

(d) α = 35°.

Figure 15.- Concluded.

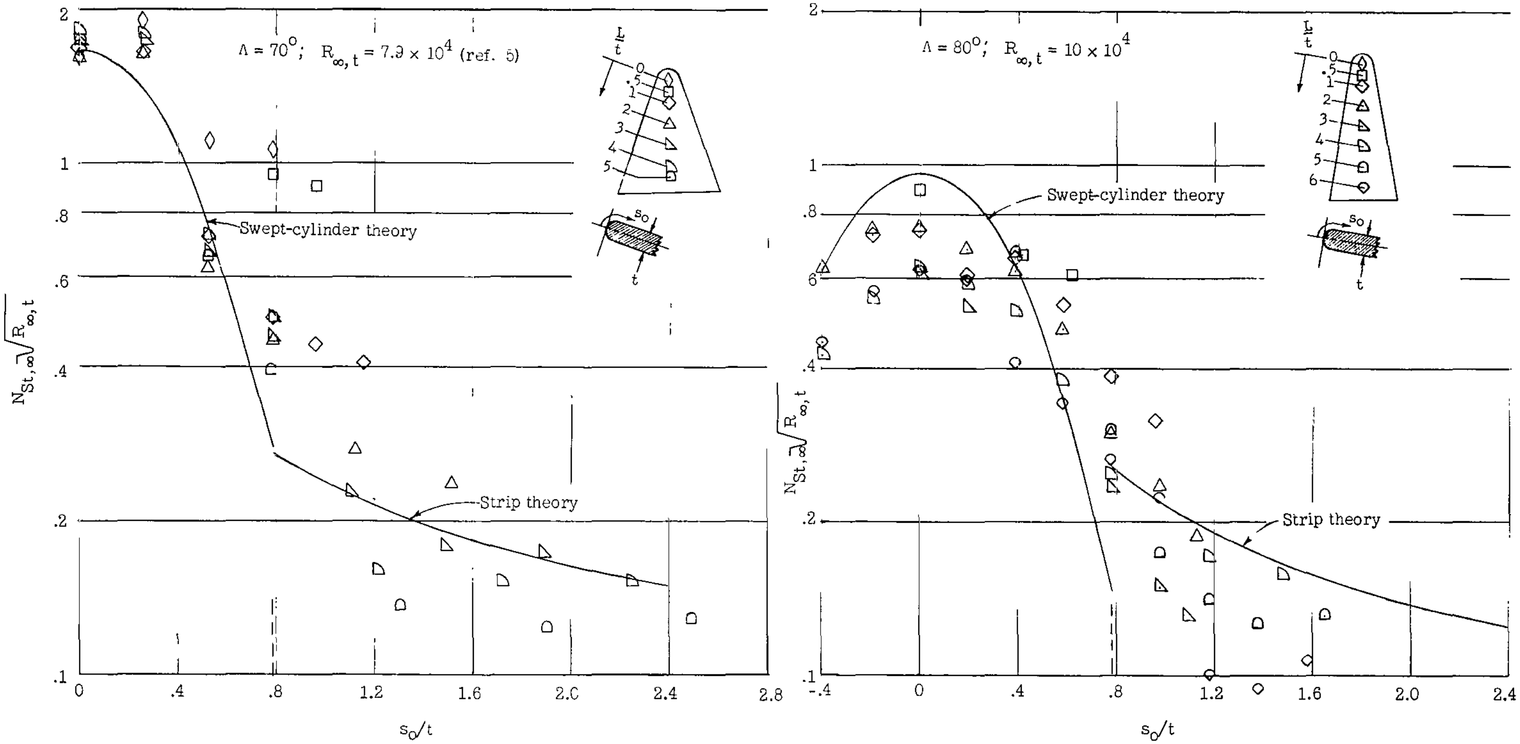

(a) α = 0°.

Figure 16.- Stanton number distribution normal to leading edge on 70° and 80° swept delta wings at various stations along leading edge at different angles of attack. $M_\infty = 9.6$.

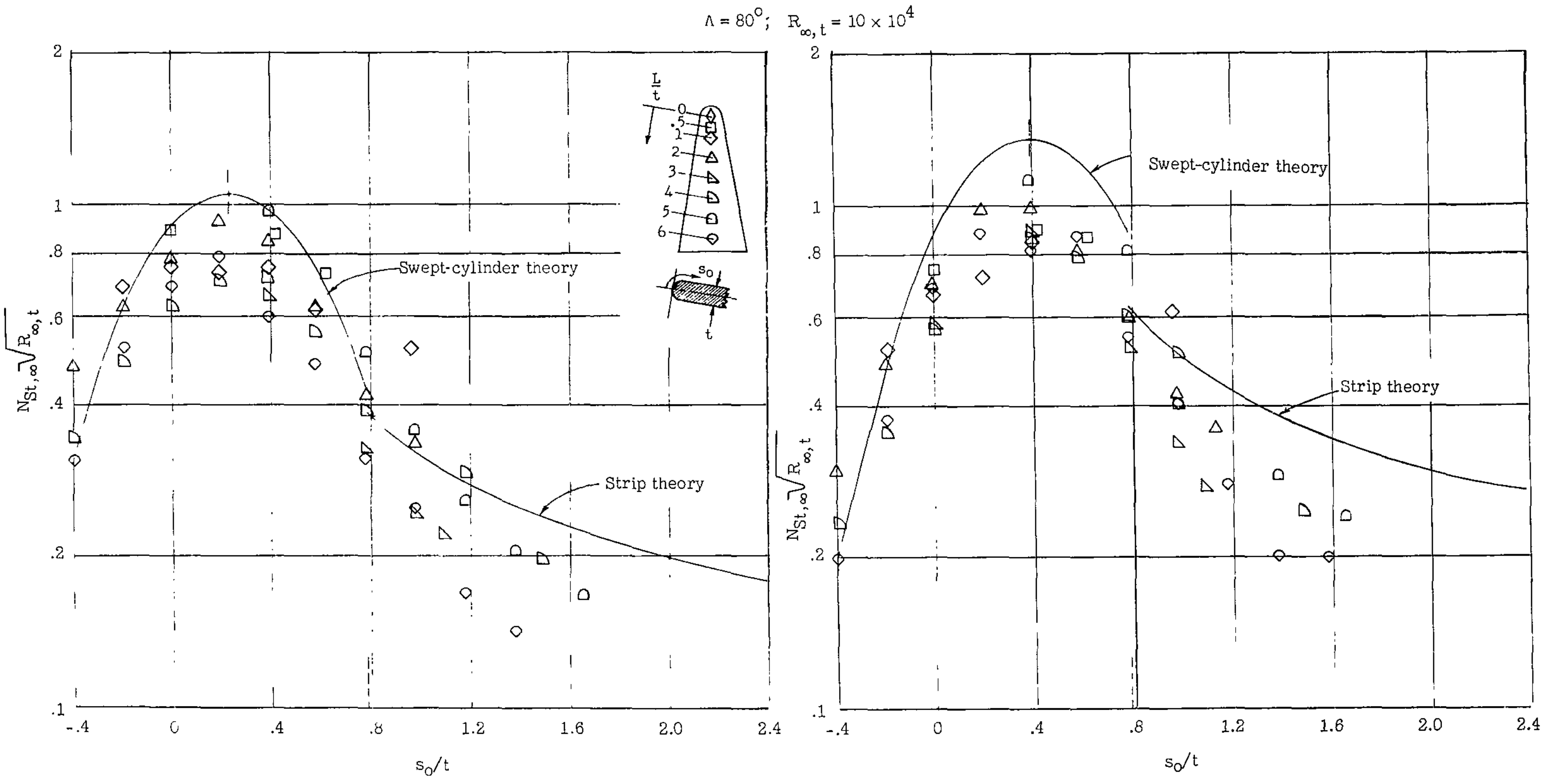

(b) α = 5°.

(c) α = 10°.

Figure 16.- Continued.

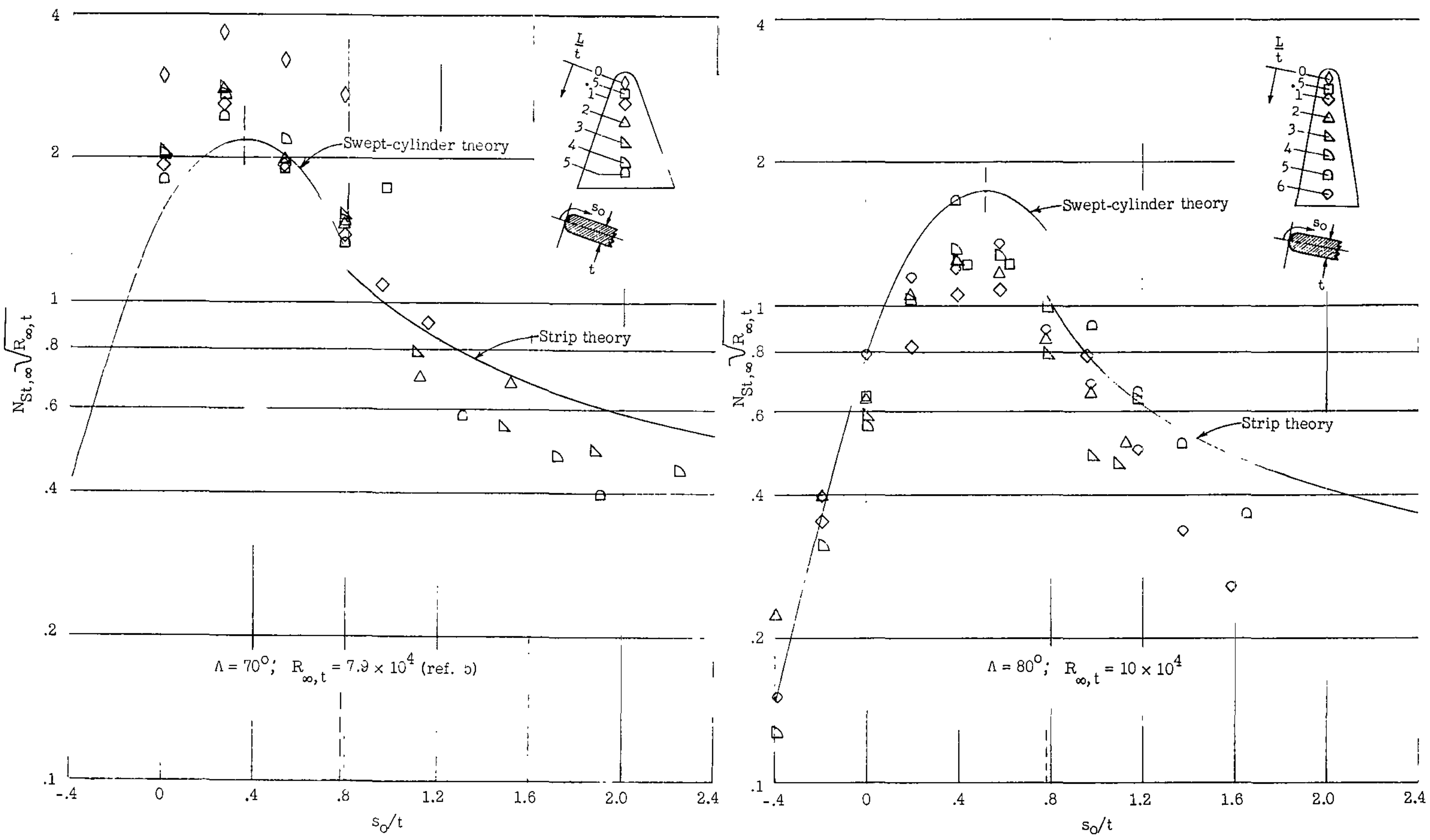

(d) α ≈ 15°.

Figure 16.- Continued.

$\Lambda = 80^\circ$; $R_{\infty,t} = 10 \times 10^4$

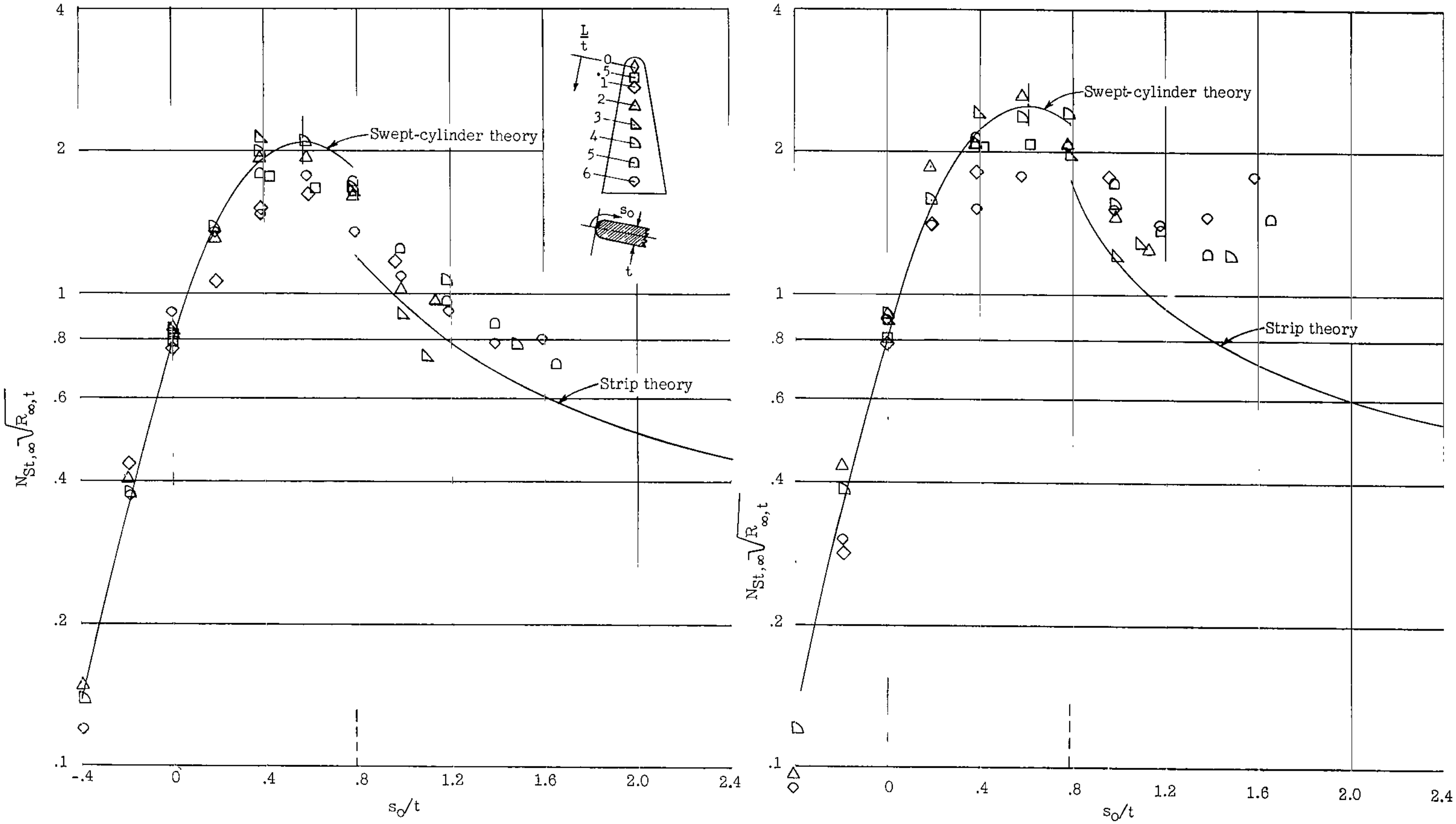

(e) $\alpha = 20^\circ$.

(f) $\alpha = 25^\circ$.

Figure 16.- Continued.

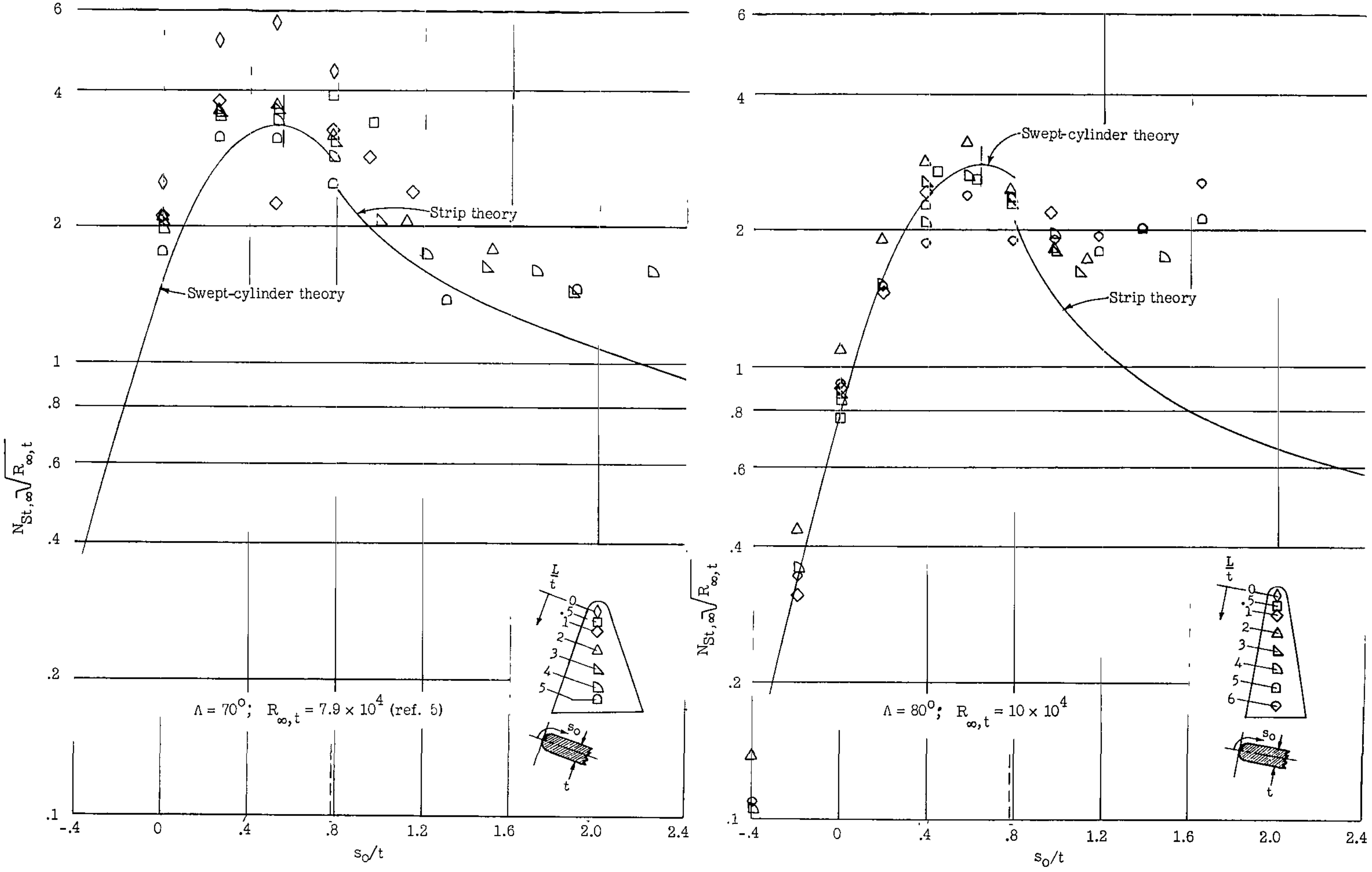

(g) $\alpha = 30^{\circ}$.

Figure 16.- Continued.

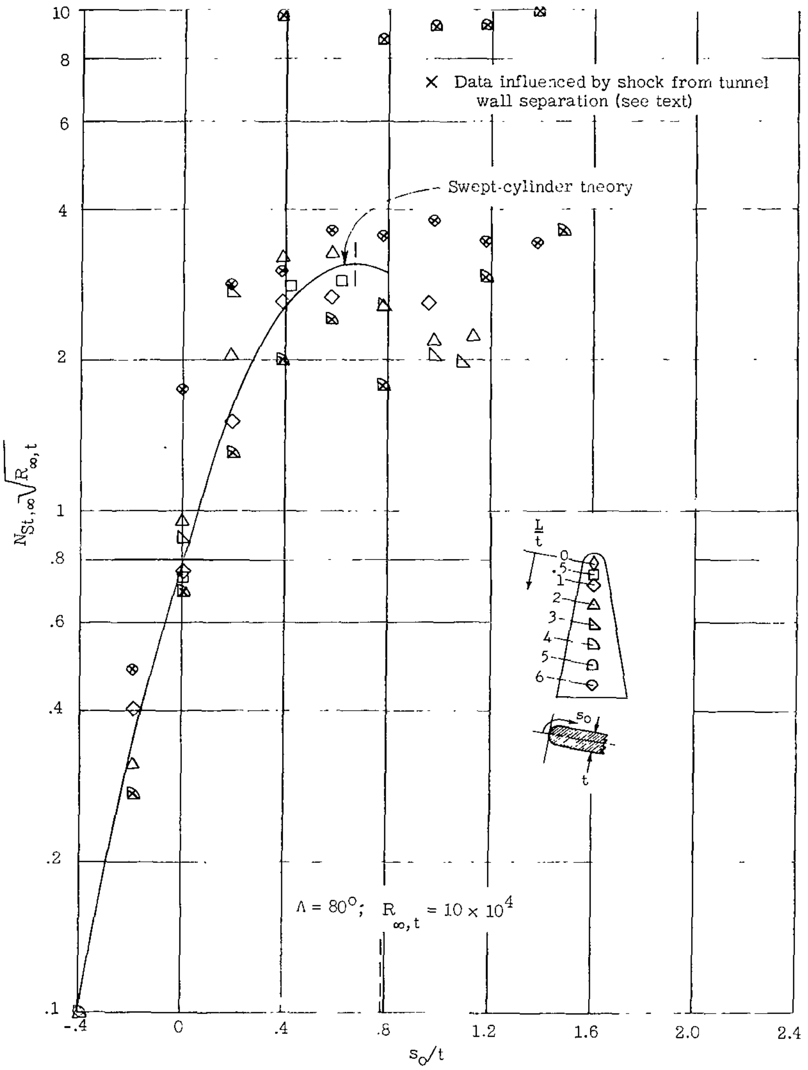

(h) $\alpha = 35^{\circ}$.

Figure 16.- Concluded.

NASA-Langley, 1965 L-4203

2/22/85

> *"The aeronautical and space activities of the United States shall be conducted so as to contribute . . . to the expansion of human knowledge of phenomena in the atmosphere and space. The Administration shall provide for the widest practicable and appropriate dissemination of information concerning its activities and the results thereof."*
>
> —NATIONAL AERONAUTICS AND SPACE ACT OF 1958

NASA SCIENTIFIC AND TECHNICAL PUBLICATIONS

TECHNICAL REPORTS: Scientific and technical information considered important, complete, and a lasting contribution to existing knowledge.

TECHNICAL NOTES: Information less broad in scope but nevertheless of importance as a contribution to existing knowledge.

TECHNICAL MEMORANDUMS: Information receiving limited distribution because of preliminary data, security classification, or other reasons.

CONTRACTOR REPORTS: Technical information generated in connection with a NASA contract or grant and released under NASA auspices.

TECHNICAL TRANSLATIONS: Information published in a foreign language considered to merit NASA distribution in English.

TECHNICAL REPRINTS: Information derived from NASA activities and initially published in the form of journal articles.

SPECIAL PUBLICATIONS: Information derived from or of value to NASA activities but not necessarily reporting the results of individual NASA-programmed scientific efforts. Publications include conference proceedings, monographs, data compilations, handbooks, sourcebooks, and special bibliographies.

Details on the availability of these publications may be obtained from:

SCIENTIFIC AND TECHNICAL INFORMATION DIVISION
NATIONAL AERONAUTICS AND SPACE ADMINISTRATION
Washington, D.C. 20546